Preprint typeset in JHEP style - HYPER VERSION IFT-UAM/CSIC-08-02, hep-ph/yymmnnn

Primordial magnetic fields from preheating at the electroweak scale

Andrés Díaz-Gil [a], **Juan García-Bellido** [a,b], **Margarita García Pérez** [a] **and Antonio González-Arroyo** [a]

[a] *Instituto de Física Teórica UAM/CSIC and Departamento de Física Teórica Universidad Autónoma de Madrid, E-28049–Madrid, Spain*

[b] *Kavli Institute for Theoretical Physics, University of California Santa Barbara, CA 93106-4030,*

E-mail: andres.diazgil@uam.es, juan.garciabellido@uam.es, margarita.garcia@uam.es, antonio.gonzalez-arroyo@uam.es

Abstract: We analyze the generation of helical magnetic fields during preheating in a model of low-scale electroweak (EW) hybrid inflation. We show how the inhomogeneities in the Higgs field, resulting from tachyonic preheating after inflation, seed the magnetic fields in a way analogous to that predicted by Vachaspati and Cornwall in the context of the EW symmetry breaking. At this stage, the helical nature of the generated magnetic fields is linked to the non-trivial winding of the Higgs-field. We analyze non-perturbatively the evolution of these helical seeds through the highly non-linear stages of symmetry breaking (SB) and beyond. Electroweak SB occurs via the nucleation and growth of Higgs bubbles which squeeze the magnetic fields into string-like structures. The W-boson charge density clusters in lumps around the magnetic strings. After symmetry breaking, a detailed analysis of the magnetic field Fourier spectrum shows two well differentiated components: a UV radiation tail at a temperature $T \sim 0.23\, m_{\rm H}$, slowly growing with time, and an IR peak associated to the helical magnetic fields, which seems to follow inverse cascade. The system enters a regime in which we observe that both the amplitude ($\rho_B/\rho_{\rm EW} \sim 10^{-2}$) and the correlation length of the magnetic field grow linearly with time. During this stage of evolution we also observe a power-law growth in the helical susceptibility. These properties support the possibility that our scenario could provide the seeds eventually evolving into the microgauss fields observed today in galaxies and clusters of galaxies.

Keywords: Inflation, preheating, primordial magnetic fields.

Contents

1. Introduction

The origin of magnetic fields (MF) is one of the remaining mysteries in relativistic astrophysics and cosmology (for reviews see the list of references [1]-[18]). Magnetic fields play an important role in the evolution of the primordial plasma in the early universe (possibly also in cosmic phase transitions), in the propagation of cosmic rays in our galaxy, as well as in clusters of galaxies. They may influence galaxy formation and large scale structures, and they may generate a stochastic background of gravitational waves. The connection between magnetic fields and gravitational waves is particularly intriguing. Since MF induce an anisotropic stress tensor, this can act as a source of gravitational waves (see [19]). Large amplitude magnetic fields from primordial turbulence could induce a significant stochastic background of gravitational waves which could be seen by LIGO or BBO, with a specific spectral signature.

Magnetic fields have been found on the scale of galaxies and clusters of galaxies with a magnitude of order the microgauss. There is even some evidence of their existence on the scale of superclusters (for a review on observational results see [20]). Summarizing the measured MF values on all scales L :

- galaxies: $B \simeq 50$ μG at $L < 1$ kpc; $B \simeq 5 - 10$ μG at $L \sim 10$ kpc.
- clusters: $B \simeq 1$ μG at $L \sim 1$ Mpc.
- superclusters: $B < 10^{-2} - 10^{-3}$ μG at $L \sim 1 - 50$ Mpc.
- CMB: $B < 10^{-3} - 10^{-5}$ μG at $L > 100$ Mpc.
- Primordial nucleosynthesis: $B < 10^{11}$ G at $T = 10^{9}$ K.

where the last bound (BBN) comes from the modification that such a background would imply for the expansion rate of the universe at primordial nucleosynthesis, which would change the observed Helium abundance.

The main difficulty in understanding the origin of magnetic fields is not in their amplitude (i.e. magnitude) but in its correlation scale, from galaxies to clusters to superclusters. The microgauss order of magnitude of present galactic MF could be explained easily from an amplification via a dynamo mechanism initiated by a tiny seed, with $B \sim 10^{-23} - 10^{-30}$ G (when taking into account gravitational collapse in a flat ΛCDM model). The explanation of the scale of the magnetic seed in this case is rather straightforward. The dynamo mechanism is an exponential mechanism which makes the MF amplitude increase a factor e at every turn of the object (typically a galaxy) with free charge and thus large electrical conductivity. Since the typical galaxy has made around 30 turns in their lifetime, the growth factor is $e^{30} = 10^{13}$. Since we observe microgauss, we just need a seed $B_{\rm seed} \sim 10^{-19}$ G over a scale of

30 kpc. This is the MF *after* gravitational collapse. Typically a galaxy forms by gravitational collapse of a lump of matter the size of about a Mpc with density of order the critical density, and ends collapsing to a size of order 30 kpc and density $\rho_{\rm gal} \sim 10^6 \rho_c$. By flux conservation, the gravitational collapse amplification gives an extra factor

$$(\rho_{\rm gal}/\rho_c)^{2/3} \sim 10^4 \,,$$

which gives a seed $B_{\rm seed} \sim 10^{-23}$ G over a scale of 1 Mpc. This calculation was done assuming matter domination. If we consider a ΛCDM universe, then gravitational collapse amplification is greater and the seed can start with $B_{\rm seed} \sim 10^{-30}$ G over a scale of 1 Mpc. This is the *minimal* value required for a typical galaxy.

The microgauss amplitude at cluster scales is more difficult to explain via a dynamo mechanism because it did not have as much time since its formation to build up from such a tiny seed, and the order of fractions of microgauss amplitude at supercluster scales is simply impossible to explain by dynamo mechanisms or gravitational collapse. In any case, even in the presence of dynamo amplification, an initial magnetic seed is required which is not provided by the dynamo mechanism itself. Theoretical models trying to account for the origin of the primordial seeds can be classified in two groups:

- Astrophysical: Biermann battery in intergalactic shocks, stellar magnetic winds (like in our Sun), supernova explosions, galactic outflows in the inter-galactic medium (IGM), quasar outflows of magnetized plasma into the intra-cluster medium (ICM), see Refs. [9, 12, 16], and a recently suggested proposal in conjunction with high energy cosmic rays [21].

- Cosmological: Early universe phase transitions [22]-[33], magnetic helicity together with the baryon asymmetry of the universe (BAU) at the electroweak (EW) transition [34]-[41], via hypercharge and hypermagnetic field generation before EW transition [42, 43], from second order cosmological perturbations from inflation [44]-[63], from preheating after inflation [64]-[67], etc.

Moreover, MF have also been observed in quasars at redshift $z \sim 2$, again with a magnitude of order the microgauss. This indicates not only ubiquity but also invariance (within an order of magnitude) with time. Such features cry for a cosmological, rather than astrophysical, origin of MF. Could it be that some yet unknown mechanism directly generated microgauss MF on all scales? The first reaction is to ask about the dynamo mechanism in galaxies, would it not amplify this microgauss MF to even larger amplitudes, as can be seen in neutron stars, and even our Sun? The surprising answer is no, because a few microgauss is the *maximum* magnetic field possible on galactic scales, due to the existence of relativistic cosmic rays and ionized gas moving at large speeds. If one computes the total energy density in cosmic

rays (integrating the measured flux spectrum over all energies), one finds

$$\frac{1}{2}\rho_{\rm CR}v^2/c^2 = 0.5 \text{ eV/cm}^3\,,$$

and a similar number for the energy density in the ionized gas moving with rotation speeds of order 200 km/s,

$$\frac{1}{2}\rho_{\rm gas}v^2/c^2 = 0.3 \text{ eV/cm}^3\,.$$

If we assume that magnetic fields are in equilibrium, due to their interaction with the cosmic rays and the gas, and furthermore we suppose equipartition, then their energy density (using 1 G $= 1.95 \times 10^{-20}$ GeV^2) becomes

$$\rho_{\rm B} = B^2/(8\pi) = 0.5 \text{ eV/cm}^3 = (5\ \mu\text{G})^2/(8\pi)\,,$$

which corresponds to a few microgauss, in surprising agreement with observations. Some people suggest that this argument may also explain the cluster MF value.

The ubiquity of MF with similar amplitude on all scales reminds us of the issue of Helium abundance in the universe. Early measurements in the fourties indicated that the Helium mass fraction to Hydrogen in the Universe was about a quarter, very nearly *everywhere*. This observation was correctly interpreted by Gamow and collaborators as indicating a primordial origin. Simple order of magnitude computation of nuclear interaction rates (mainly those of deuterium, a necessary step in the reactions from H to He) and comparison with the rate of expansion in the early universe at temperatures of order the nuclear transitions (i.e. MeV), together with the then largely unknown neutron decay rate, suggested that the present abundance of Helium could have been produced from Hydrogen in the early universe and thus be present everywhere. The other light elements seemed to require further synthesis in stars and thus depended on location, but the Helium was ubiquitous because it was there from the very beginning.

Something similar may have happened with magnetic fields, if they were generated in the early universe by some unknown mechanism and then redshifted until today. The question is what is the typical energy density which today gives the order microgauss fields? These fields (if homogeneous) redshift as radiation, i.e. $\rho_{\rm B}(a) = \rho_{\rm B}(\text{today})(a_0/a)^4$. Like with Helium, we have to ask what was the energy scale of interactions responsible for the generation of primordial magnetic fields? Photons are massless so in principle any scale, as long as there are charged particles, is sufficient to generate magnetic fields, and this is the reason why there is still so much debate as to their origin. However, was the universe always permeated with electromagnetic waves? The answer is no, the electromagnetic interaction as we know it came into being at a very precise time, when the electroweak (EW) force broke into the weak interactions plus electromagnetism. Before we could not talk

about photons and magnetic fields. This occurred when the typical energy (or temperature) in the universe was around $T_{\rm EW} \sim 100$ GeV. If we construct an energy density with this scale we get $\rho_{\rm EW} \sim 10^8$ GeV^4. At that time the universe was (or became) radiation dominated. If we now redshift this MF energy density until today ($T_0 = 2.725$ K) we get

$$\rho_{\rm B}({\rm today}) = (T_0/T_{\rm EW})^4 \rho_{\rm EW} \sim 3.04 \times 10^{-53}\ {\rm GeV}^4 = 0.4\ {\rm eV/cm}^3$$

which is *precisely* the order of magnitude of the present MF energy density.[1] This would be enough to explain the cluster and supercluster values, and would perhaps require a mild dynamo mechanism to grow to galactic values (if the fraction $f \ll 1$). The question is whether this is just a coincidence or it is hinting directly at its origin.[2] While other mechanisms require a seed with an arbitrary scale (typically $B \sim 10^{-23}$ G, so that today we observe microgauss MF on galactic scales via the dynamo mechanism), there is no physical reason behind this scale. On the other hand, the EW scale is a *natural* scale for the generation on magnetic fields since it is the scale at which electromagnetism arises for the first time as a fundamental interaction.

Whether this is sufficient reason to assign the EW energy scale to the origin of magnetic fields is another issue. In particular, it is not clear how to obtain the large correlation length of magnetic fields observed at galactic and cluster scales. Any physical mechanism that creates magnetic fields must be necessarily causal, but at high temperatures in the early universe there is also a natural coherence scale given by the particle horizon. At the electroweak scale the physical horizon is 10^{-10} light-seconds (~ 3 cm), which today corresponds to a co-moving scale of 0.3 mpc (~ 1 AU), clearly insufficient when compared even with the irregular (turbulent) component of the galactic magnetic field ($L \sim 100$ pc), not to mention the regular (uniform) component, which has correlations $L \sim 10$ kpc. It thus seems impossible to explain the coherent magnetic fields observed on galaxy clusters and supercluster scales (of order 10 Mpc) with intensities of order μG to nG.

There is however a second coincidence, which makes things even more intriguing. If we assume that the plasma after the electroweak transition is sufficiently turbulent to maintain magnetic fields of the largest possible coherence scales via inverse cascade [29]-[33], then we could reach cosmological scales today. Let us follow the argument. The largest coherence scale at the electroweak transition is the physical horizon, of order 3cm. If a strong inverse cascade is active, then the coherence length of the magnetic fields will grow as fast as the horizon (it cannot grow faster). This means

[1] We could be even more conservative and suppose that the fraction of magnetic field energy density to radiation at the time of the EW transition was given by $f = \rho_{\rm B}/\rho_{\rm rad} < 1$. In this case, the present MF magnitude would be $B_0 \sim 5\, f^{1/2}\ \mu$G.

[2] Some authors suppose that the generation occurred *earlier* in the form of hypermagnetic fields and was then converted into ordinary magnetic fields at the EW scale [43].

that it grows like the scale factor *squared* during the radiation dominated era. This ideal situation could only last while there is a plasma and thus it is bound to stop acting at photon decoupling, when the universe becomes neutral. Since then, the correlation length can only grow with the expansion of the universe, as the scale factor. If we take this effect into account from the electroweak scale until today we find, using the adiabatic expansion relation $T \propto a^{-1}$,

$$\xi_0 = \xi_{\rm EW} \left(\frac{a_{\rm dec}}{a_{\rm EW}}\right)^2 \frac{a_0}{a_{\rm dec}} = 3\,{\rm cm} \left(\frac{T_{\rm EW}}{T_{\rm eq}}\right)^2 \frac{T_{\rm eq}}{T_0} \sim 6 \times 10^{25}\,{\rm cm} = 20\ {\rm Mpc}\,, \qquad (1.1)$$

where we have made the approximation that equality and decoupling occurred more or less simultaneously (a careful computation gives only a minor correction). The surprising thing is that this simple calculation gives *precisely* the order of magnitude for the largest correlation length of cosmic MF ever observed (i.e. cluster scales). If the agreement in the magnitude of the primordial MF seed seemed peculiar, the fact that an inverse cascade could also be responsible for the observed correlation length becomes a surprising coincidence, probably hinting at an underlying mechanism. It is therefore worthwhile exploring the conditions that could have taken place at the electroweak transition which could give rise to a significant fraction of energy density in magnetic fields, and be responsible for a sustained period of inverse cascade until photon decoupling. It has been shown in Refs. [30]-[33] that one important ingredient is the generation of magnetic fields with a non trivial helical component, which guarantees an optimal amplification of the magnetic correlation length through inverse cascade. A very good account of the large number of works investigating these issues, with a complete list of references is given in Ref. [9] (see also [27]-[43]).

In this paper we propose a scenario in which the electroweak transition takes place at the end of a brief period of hybrid inflation[3] It has been conjectured that preheating and early reheating in this model could provide an alternative mechanism to generate the baryon asymmetry in the universe [70]-[76] and a way to source gravitational waves [77]. In this paper we analyze whether it could also give rise to primordial magnetic fields with the required amplitude and correlation length. This issue has been partially addressed in a recent letter [78]. Here we will present a complete account of the results obtained and a detailed description of the approach employed in the analysis. Our set up provides a specific realization of some of the proposals described above. In particular, we will see how helical magnetic fields arise from the inhomogeneities in the spatial distribution of the Higgs field, along the lines conjectured by Vachaspati [34, 36] and Cornwall [38] some years ago.

The paper is organized as follows. In section 2 we describe the hybrid inflation model that we will be using and revise, following Ref. [73], how to solve the quan-

[3]Note that we do not need a 60 e-fold period of inflation, just a few ($\sim$ 5) e-folds of low scale thermal inflation [68, 69] to cool down the universe. The amplitude of CMB temperature fluctuations would be determined by the usual 55 e-folds of high-scale (e.g. GUT) inflation.

tum evolution of the system from the end of inflation until non-linearities start to become important. Beyond this time, a fully non-perturbative approach is required. Fortunately, the time evolution at this stage can be described within the classical approximation as demonstrated in Ref. [73]. Details on the methodological set up and the lattice implementation are presented in section 3. Section 4 analyzes the mechanism leading to helical magnetic fields following from the inhomogeneities in the Higgs field, which are seeded by the Higgs quantum fluctuations that arise from the period of linear quantum evolution. Strings of magnetic flux, carrying non-vanishing helicity, are clearly observed. They persist and are even enhanced as the system progresses towards the true vacuum. We also analyze here the structure of the plasma of $W-$charges which accompany the magnetic fields during this period. The fate of these magnetic fields at later times is discussed in section 5, where we present a detailed study of the spectrum of the magnetic field. We will show that there is a significant helical magnetic field remnant whose amplitude and correlation length are amplified linearly in time. In section 6 we will discuss lattice and finite volume independence of our results, as well as the dependence of magnetic field production on the Higgs- to W-mass ratio. Conclusions and prospects for further work are presented in section 7. Finally, a few technical points about the lattice discretization of the classical equations of motion, the Maxwell equations and electromagnetic radiation are described in the Appendices A, B and C. Appendix D is devoted to an analysis of the Gaussian random fields that provide the initial Higgs field distribution.

2. The model

The scenario we will be considering is that of preheating after a period of hybrid inflation which ends at the EW scale. This was first introduced in Ref. [70] to provide a new mechanism for the generation of baryon asymmetry in the Universe (BAU). It has been extensively studied since then both in connection with BAU [70]-[76] and in relation with the production of gravitational waves [77]. In this paper and in Ref. [78] we include for the first time the Hypercharge field in order to study the generation of electromagnetic fields during preheating (preliminary results can be found in [79]). In this section we will introduce the model and describe the first stages of evolution after inflation ends which provide the initial conditions for the non-linear approach addressed in section 3.1.

The Hybrid inflation model is attained by extending the Standard Model with the addition of a scalar field, the inflaton, singlet under the gauge group. The scalar sector thus includes the Higgs field: $\Phi = \frac{1}{2}(\phi^0 \, \mathbb{1} + i\phi^a \tau_a)$ (τ_a are the Pauli matrices) and the singlet inflaton χ which couples only to the Higgs via the scalar potential:

$$\mathrm{V}(\Phi,\chi) = \mathrm{V}_0 + \frac{1}{2}(g^2\chi^2 - m^2)\,|\phi|^2 + \frac{\lambda}{4}|\phi|^4 + \frac{1}{2}\mu^2\chi^2\,, \tag{2.1}$$

where $|\phi|^2 \equiv 2\mathrm{Tr}\,\Phi^\dagger\Phi$, μ is the inflaton mass in the false vacuum and $m_{\scriptscriptstyle\mathrm{H}} = \sqrt{2}\,m \equiv \sqrt{2\lambda}\,v$ the Higgs mass, with $v = 246$ GeV the Higgs vacuum expectation value at the electroweak scale. The gauge sector contains both the SU(2) and the hypercharge U(1) fields with

$$\mathcal{G}^a_{\mu\nu} = \partial_\mu \mathcal{A}^a_\nu - \partial_\nu \mathcal{A}^a_\mu + g_{\scriptscriptstyle\mathrm{W}} \epsilon^{abc} \mathcal{A}^b_\mu \mathcal{A}^c_\nu \tag{2.2}$$

and

$$\mathcal{F}^{\scriptscriptstyle\mathrm{Y}}_{\mu\nu} = \partial_\mu \mathcal{B}_\nu - \partial_\nu \mathcal{B}_\mu, \tag{2.3}$$

their respective field strengths. The covariant derivative is:

$$\mathcal{D}_\mu = \partial_\mu - \frac{i}{2} g_{\scriptscriptstyle\mathrm{W}} \mathcal{A}^a_\mu \tau_a - \frac{i}{2} g_{\scriptscriptstyle\mathrm{Y}} \mathcal{B}_\mu, \tag{2.4}$$

with $g_{\scriptscriptstyle\mathrm{W}}$ the SU(2) gauge coupling and $g_{\scriptscriptstyle\mathrm{Y}}$ the hypercharge coupling. In this work we can safely ignore fermionic fields since the time scales involved in the perturbative decay of the Higgs field into fermions are much larger than the ones considered here.

With all these definitions the Lagrangian density of the model becomes:

$$\mathcal{L} = -\frac{1}{4}\mathcal{G}^a_{\mu\nu}\mathcal{G}^{\mu\nu}_a - \frac{1}{4}\mathcal{F}^{\scriptscriptstyle\mathrm{Y}}_{\mu\nu}\mathcal{F}^{\mu\nu}_{\scriptscriptstyle\mathrm{Y}} + \mathrm{Tr}\Big[(\mathcal{D}_\mu\Phi)^\dagger \mathcal{D}^\mu \Phi\Big] + \frac{1}{2}\partial_\mu\chi\partial^\mu\chi - V(\Phi,\chi)\,. \tag{2.5}$$

For our analysis we have fixed the W mass and the Z to W mass ratio to the experimental values [80]. We have analyzed three different values of the Higgs to W mass ratio: $m_{\scriptscriptstyle\mathrm{H}}/m_{\scriptscriptstyle\mathrm{W}} = 2\sqrt{2\lambda}/g_{\scriptscriptstyle\mathrm{W}} = 2$, 3 and 4.65. The Higgs-inflaton coupling has been fixed to $g^2 = 2\lambda$ as in super-symmetric models [71, 81] and we have taken the inflaton bare mass $\mu = 10^{-5} g v \approx 0$.

The extraction of the electromagnetic content of the SU(2)×U(1) fields in the Lagrangian proceeds in the usual way. Fixing the unitary gauge, $\Phi(x) = \rho(x)\,\mathbb{1}$, the Z-boson field and the electromagnetic field are extracted from appropriate orthogonal combinations of the SU(2) and hypercharge vector potentials:

$$\mathcal{Z}_\mu(x) = \cos\theta_W\,\mathcal{A}^3_\mu(x) + \sin\theta_W\,\mathcal{B}_\mu(x)\,, \tag{2.6}$$

$$\mathcal{A}^\gamma_\mu(x) = \sin\theta_W\,\mathcal{A}^3_\mu(x) - \cos\theta_W\,\mathcal{B}_\mu(x)\,. \tag{2.7}$$

with $\varphi(x) = \Phi(x)(1,0)^{\mathrm{T}}$ the Higgs doublet. This separation can only be done unambiguously when the Higgs field is on the true vacuum, i.e. in the broken symmetry phase. However even in that phase there can be points where the Higgs field vanishes and the symmetry is locally restored (a typical example of a configuration exhibiting such behavior is the sphaleron). At those points there is no unique way to define the electromagnetic fields. In fact 't Hooft was the first to point out in Ref. [82] the consequences of this ambiguity in the Georgi-Glashow model, tying it to the appearance of non-trivial configurations like monopoles or strings, acting as sources of magnetic fields. In Ref. [34] Vachaspati pointed out that a similar mechanism was at work in the electroweak model where the sources for magnetic field generation are tied to the

presence of non-homogeneous phases in the Higgs field. In the following sections we will analyze in detail how this mechanism is realized during the period of preheating after inflation.

2.1 Linear quantum evolution

Following Refs. [73, 74], we will address here the first stages of evolution starting at the end of inflation.

The period of inflation is characterized by the fact that the Higgs and inflaton fields are displaced from the true minimum of the potential. In this case, inflation is driven by the false vacuum energy, $V_0 = \lambda v^4/4$. During this time the inflaton homogeneous mode, $\chi_0 \equiv \langle\chi\rangle$, dominates the dynamics. After only about 5-10 e-folds the Universe has cooled down and all other particle species have been diluted, remaining in the de Sitter vacuum.[4]

The interaction between the Higgs and inflaton fields drives the end of inflation and triggers EW symmetry breaking. The way this proceeds is as follows. Close to the time when inflation ends, denoted by t_c, the time evolution of the inflaton zero mode can be approximated by:

$$\chi_0(t) = \chi_c(1 - Vm(t - t_c)) \tag{2.8}$$

where $\chi_c = \chi_0(t_c) \equiv m/g$. Here V denotes the inflaton dimensionless velocity, defined through this equation and fixed to $V = 0.024$ in our analysis [73]. The variation of $\chi_0(t)$ induces, via the Higgs-inflaton coupling, a time dependence of the effective Higgs mass parameter, $m_\phi^2 = -M^3(t - t_c) \equiv -2Vm^3(t - t_c)$, which changes from positive to negative, triggering electroweak symmetry breaking. Accordingly, the time when inflation ends, t_c, is characterized as the critical point where the Higgs field becomes massless.

As described in detail in Refs. [73, 74], it is possible to solve exactly the quantum evolution of the system around t_c if non-linearities in the Higgs field and the interaction with the gauge fields are neglected. As we will see below, this is a reasonable assumption at this stage. In this approximation the Higgs field is effectively described as a free scalar field with a time dependent mass $m_\phi(t)$. Its quantum evolution can be solved in terms of Airy functions [73]. After t_c, low momentum modes of the Higgs field grow exponentially in a process known as "tachyonic preheating" [71]. Due to the tachyonic growth, low momentum Higgs field modes acquire large occupation numbers and, soon after t_c, they evolve as classical modes. This is a very fast process so that all other modes can be taken to remain in the quantum vacuum (ground) state, justifying thus the linear approximation. These modes will be later populated through the interaction with the Higgs field tachyonic modes. Once non-linearities

[4]For electroweak-scale inflation and the range of momenta we will be considering, de Sitter vacuum is indistinguishable from the Minkowski vacuum.

start to become relevant the approximation ceases to be valid and a full non-linear treatment is required. Our strategy for dealing with the later stages of evolution will be presented in the next section.

3. Methodological set up

Beyond the quantum linear evolution described in the previous section we have to deal with the non-linear dynamics of the Higgs field and its coupling to the gauge fields. Our approach is based upon the classical approximation (details can be found in [73, 74] - see also [76]). The validity of this approximation relies on the fast growth of tachyonic modes as explained previously. In what follows we will describe several aspects of our procedure.

3.1 Initial conditions for the the non-linear evolution

As mentioned previously the initial stages after the end of inflation ($t = t_c$) lead to a rapid growth of the tachyonic modes which tend to behave classically. The correlation functions of the Higgs field resulting from the initial quantum evolution can be computed. Our approach is to use these results as initial conditions for the classical evolution of the system. The quantum fluctuations translate into stochastic initial conditions for the Higgs field, whose correlations are designed to match the Weyl-ordered quantum expectation values. The matching of the two methods is done at an initial time $t = t_i > t_c$ that must be large enough for classical behaviour to set in and small enough to make the non-linear terms small. This leaves a window of possible values of t_i. We tested the robustness of the results with respect to changes in t_i within these limits, giving confidence on the self-consistency of our approach.

Given the linear character of the initial quantum evolution, the Higgs field momentum modes ϕ_k^α, at $t = t_i$ behave as Gaussian random variables of zero-mean following a Rayleigh distribution:

$$\exp\Big(-\frac{|\phi_k^\alpha|^2}{(\sigma_k^\alpha)^2}\Big)\,\frac{d|\phi_k^\alpha|^2}{(\sigma_k^\alpha)^2}\,\frac{d\theta_k^\alpha}{2\pi}\,, \tag{3.1}$$

where θ_k^α is the phase of the complex random variable ϕ_k^α. The dispersion of the modulus is expressed in terms of the power spectrum $P(k,t_i) = k^3(\sigma_k^\alpha)^2$, and can be computed analytically in terms of Airy functions [73]. For practical purposes it is better to work with a simple functional fit to the power spectrum (Eq. (D.1)). Notice that we have introduced a momentum cut-off, removing modes which have not become tachyonic (classical). As explained in Ref. [73], this is compensated by a renormalization of the parameters.

The study of the properties of this 4-component Gaussian random field is collected in Appendix D. Its features depend on several parameters: the Higgs mass, the initial inflaton velocity V, the momentum cut-off and the choice of initial time

t_i. The first two appear combined in a new scale $M = (2V)^{1/3}m$ characteristic of the initial linear evolution. The main conclusion drawn in Appendix D, is that to a large extent all these parameter dependencies translate into setting two main scales: a spatial length scale, ξ_0, and the Higgs dispersion, σ, which determines the magnitude of the Higgs field.

More specifically, in Appendix D we study the distribution of local maxima in $|\phi(x)|$. These "peaks" are the seeds that will later grow with time and develop into bubbles which start expanding and colliding among themselves once the Higgs fields enters the non-linear regime characteristic of symmetry breaking. This process was described in detail in Ref. [73]. Note that the multicomponent character of the Higgs field affects the results but, more importantly, it gives rise to new observables, some of which are intimately connected to the physical phenomena which are the main goal of this paper. This will be described in the next section.

To complete the description of the initial conditions, we mention that, similarly to the high-momentum modes of the Higgs field, all other non-tachyonic modes are set to zero. These include the non-homogeneous modes of the inflaton and the vector potentials of the SU(2) and hypercharge gauge fields. The initial time-derivatives of these quantities are also set to zero except for the gauge fields which have to be chosen such that the Gauss constraint is satisfied as an initial condition. The dynamic equations guarantee that the constraint will continue to hold at later times. The aforementioned robustness of the results to the choice of initial time t_i implies that our physical conclusions do not depend on minor modifications of these initial conditions.

3.2 Numerical procedure

In order to study the non-linear evolution of the system with our stochastic initial conditions we have made use of the lattice approach. This has the advantage that classical equations of motion are discretized preserving full gauge invariance of the system. Generally speaking the procedure is standard. Details on the lattice Lagrangian and the lattice form of the equations of motion are presented in Appendix A. At early times the errors associated to discretization are very small due to the cut-off form of the initial spectrum. This shows up in the very mild dependence of the results on the spatial a and temporal a_t lattice spacings. This contrasts with other situations in which lattice techniques have been used. As time evolves higher momenta of the fields grow and start to play a role, eventually leading to a breakdown of the approximation. We have explicitly analysed that this does not occur for the range of times covered in this paper. A different approach needs to be followed if one wishes to reach times in which full thermalisation has been reached. Notice, however, that this goal also demands the introduction of fermionic degrees of freedom which can be safely ignored in our time span. Our present results can be used as initial conditions for the study of the late time behaviour of the system.

Another approximation needed for the numerical procedure is to put the system in a box with periodic boundary conditions. The physical volume, $\mathcal{V} = L^3$ is given in terms of the minimum momentum: $L = 2\pi/p_{\min}$. The latter has to be chosen judiciously to lie well within the tachyonic band of the Higgs field. The dependencies of the results can be monitored by using different values for the parameters of the simulation. In Table 1 we enumerate the different lattice sizes, spacings and physical volumes that we have used.

N_s	ma	ma_t	$p_{\min}/m$
64	0.65	1/40	0.150
80	0.52	1/40	0.150
100	0.42	1/40	0.150
100	0.52	1/40	0.125
100	0.65	1/40	0.100
120	0.65	1/40	0.080

Table 1: List of lattice parameters: a and a_t are respectively the spatial and temporal lattice spacings, N_s is the number of lattice points and $p_{\min} = 2\pi/(N_s a)$ is the minimum momentum. The $N_s = 120$ lattice has only been used for the study of the initial configuration. The number of different configurations of each lattice ranges from 80 to 200, depending of the lattice and the choice of parameters.

Due to its relevance for the goals of our paper, we will now explain in detail how the electromagnetic and Z fields are defined in our lattice approach. This can only be done unambiguously when the Higgs field is in the true vacuum, i.e. in the broken symmetry phase. One can compute, in a gauge invariant way, the field associated to the Z-boson potential as:

$$Z_\mu(m) = \frac{-i\mathrm{Tr}\Big[\hat{n}(D_\mu\Phi(m))\Phi^\dagger(m)\Big]}{|\phi(m)||\phi(m+\mu)|} \tag{3.2}$$

$$\equiv -i\mathrm{Tr}\Big[\tau_3\frac{\Phi^\dagger(m)}{|\phi(m)|}U_\mu(m)\frac{\Phi(m+\mu)}{|\phi(m+\mu)|}B_\mu(m)\Big] \xrightarrow{a\to 0} \quad a_\mu g_Z \mathcal{Z}_\mu(x)\,, \tag{3.3}$$

where we have introduced the adjoint unit vector $\hat{n} = n_a\tau_a$, with components:

$$n_a(x) = \frac{\varphi^\dagger(x)\tau_a\varphi(x)}{|\varphi(x)|^2}\,, \tag{3.4}$$

with $\varphi(x) = \Phi(x)(1,0)^{\mathrm{T}}$ the Higgs doublet. The Z boson coupling is denoted by g_Z and $a_i = a$, $a_0 = a_t$. D_μ is the lattice covariant derivative operator defined in Eq. (A.6) of Appendix A. $U_\mu(n)$ and $B_\mu(n)$ are, respectively, the SU(2) and hypercharge link fields introduced in Appendix A. Notice that continuum quantities are defined with calligraphic letters to distinguish them from the lattice quantities. Our definition of the Z boson potential corresponds to the standard one in the unitary gauge.

We define the Z boson and hypercharge field strengths through the clover averages [5]

$$F^{\rm Z}_{\mu\nu}(m) = \langle \Delta_\mu Z_\nu(m) - \Delta_\nu Z_\mu(m) \rangle_{\rm clov} \xrightarrow{a\to 0} a_\mu a_\nu g_Z \mathcal{F}^Z_{\mu\nu}(x) + \mathcal{O}(a^4) \tag{3.5}$$

and

$$F^{\rm Y}_{\mu\nu}(m) = \langle \Delta_\mu \theta_\nu(m) - \Delta_\nu \theta_\mu(m) \rangle_{\rm clov} \xrightarrow{a\to 0} a_\mu a_\nu g_{\rm Y} \mathcal{F}^Y_{\mu\nu}(x) + \mathcal{O}(a^4)\,, \tag{3.6}$$

where $B_\mu(m) \equiv \exp(i\theta_\mu(m)\tau_3/2)$ is the hypercharge link, Δ_μ is the lattice derivative operator introduced in Eq. (A.8) and $\langle O \rangle_{\rm clov}$ denotes the clover averages defined in Eqs. (B.2)-(B.3). In terms of them we can compute the lattice electromagnetic field strength as:

$$F^\gamma_{\mu\nu}(n) = \sin^2(\theta_W) F^{\rm Z}_{\mu\nu}(n) - F^{\rm Y}_{\mu\nu}(n) \xrightarrow{a\to 0} a_\mu a_\nu e \mathcal{F}^\gamma_{\mu\nu}(x) + \mathcal{O}(a^4)\,, \tag{3.7}$$

where $\mathcal{F}^\gamma_{\mu\nu}$ is the corresponding continuum electromagnetic field strength. This provides a lattice gauge invariant definition of the electromagnetic field which is equivalent to the usual definition in the unitary gauge.

4. The mechanism underlying magnetic field generation

In this section we study the production of magnetic fields during the first stages of our EW preheating scenario. This analysis is performed in two steps. The first is to investigate the presence, size and structure of the magnetic fields generated by our Gaussian random field initial distribution. This complements the results presented in Appendix D. Then we will track the evolution of these magnetic fields through the highly non-linear stages associated to EW symmetry breaking. This is a crucial period where there are no viable alternatives to our methodological approach.

4.1 Initial Magnetic fields

A close look at our expression of the photon field reveals that Abelian electromagnetic fields are present in the first stages of the evolution. The discussion on how this comes about follows a line of argument very similar to that developed by Vachaspati in Ref. [34]. The tachyonic preheating phase leads to a multicomponent Gaussian Higgs field. The SU(2) and hypercharge gauge fields remain very small. This is incorporated into our initial conditions by setting the hypercharge and SU(2) magnetic-like fields to zero and fixing the corresponding electric fields in order to satisfy the Gauss constraint. We work in the $A_\mu = 0$ gauge, which on the lattice corresponds to $U_\mu(t = t_i) = B_\mu(t = t_i) = \mathbb{1}$. Projecting onto the Z and electromagnetic fields we

[5] Corrections to the continuum approach of the time-space clover averages are order $\mathcal{O}(a_0 a^2)$.

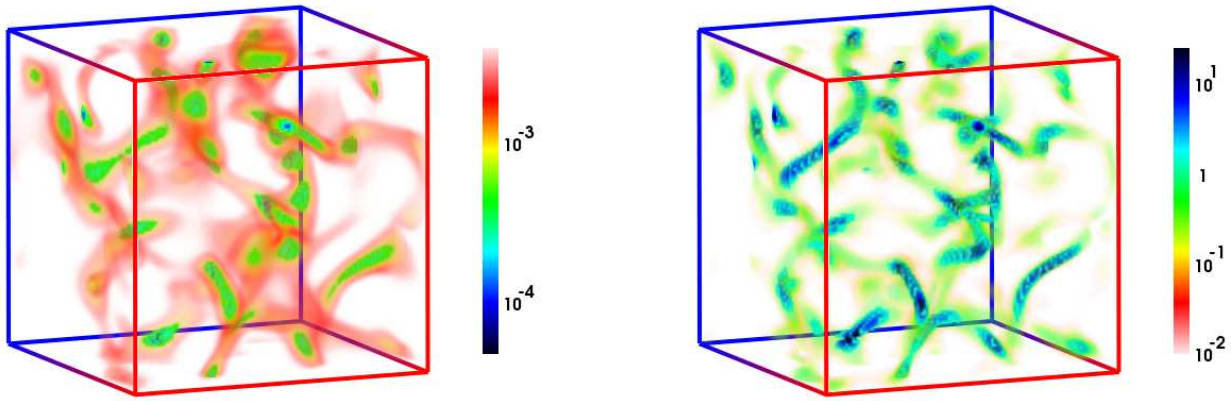

Figure 1: (Left) Locus of points where the value of the Higgs field norm is below $0.03\,v$. (Right) Locus of points where twice the magnetic energy density ($|\vec{B}|^2$) is above $0.03\,m^4$. Data correspond to $mt = 5$ and $m_{\rm H} = 2m_{\rm W}$.

obtain:

$$\mathcal{Z}_\mu(x) = \frac{i}{g_z}\,\mathrm{Tr}\left[\,\hat{n}\,\Omega(x)\partial_\mu\Omega^\dagger(x)\,\right] \tag{4.1}$$

$$\mathcal{F}^{\rm Z}_{\mu\nu}(n) = \frac{i}{g_z}\,\mathrm{Tr}\left[\,\hat{n}\left(\partial_\nu\Omega(x)\partial_\mu\Omega^\dagger(x) - \partial_\mu\Omega(x)\partial_\nu\Omega^\dagger(x)\right)\right]$$

$$\mathcal{F}^{\gamma}_{\mu\nu}(x) = \tan\theta_W\mathcal{F}^{\rm Z}_{\mu\nu}(x) \equiv \frac{i\sin\theta_W}{g_W}\,\mathrm{Tr}\left[\,\hat{n}\left(\partial_\nu\Omega(x)\partial_\mu\Omega^\dagger(x) - \partial_\mu\Omega(x)\partial_\nu\Omega^\dagger(x)\right)\right],$$

expressed in terms of the SU(2) matrix:

$$\Omega(x) = \frac{\Phi(x)}{|\phi(x)|}\,. \tag{4.2}$$

It becomes clear that electromagnetic fields are sourced by the presence of inhomogeneities in the Higgs field orientation. This is one of the essential ingredients in Vachaspati's proposal for magnetogenesis.

The size and spatial distribution of this initial electromagnetic and Z fields can be obtained from the multicomponent Gaussian random field. In Appendix D we displayed the histogram of magnetic field values. Here we will focus on another aspect which is particularly interesting for the later evolution. This is the spatial distribution of points where the magnetic field intensity is larger. To investigate this, we show in Fig. 1 a 3-dimensional plot displaying the locus of points where the magnetic energy density is above 0.03 m^4 for our initial configuration at $mt_i = 5$. Notice that the regions of higher magnetic energy density exhibit a string-like geometry.

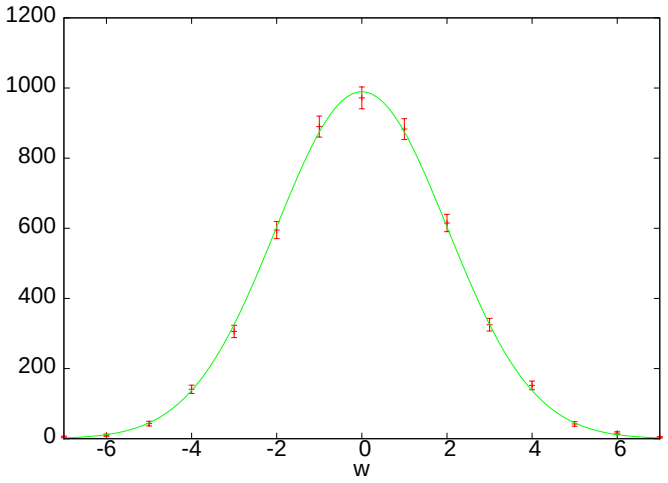

Figure 2: Histogram of Higgs winding number for the initial configuration $mt = 5$ for $p_{\min} = 0.15\, m$.

Indeed, this spatial distribution tracks the location of regions of low Higgs field value, which are also presented in the figure. Although, the strings seem to end at certain spatial points, this is simply a reflection of the spreading of magnetic flux lines. Our electromagnetic field satisfies the Maxwell equations without magnetic sources or sinks. According to our formulas the initial magnetic-like component of the Z-boson field strength is directly proportional to the electromagnetic field and has identical structure.

There is another important feature of magnetic fields which we have investigated. It corresponds to whether the initial field gives rise to a sizable helicity. In a finite volume the total magnetic helicity is defined both in configuration and in momentum space as:

$$H \equiv \int d^3x\; h(x) = \int d^3x\, \vec{A}\cdot\vec{B} \equiv \frac{-i}{\mathcal{V}} \sum_k \frac{\vec{k}}{|\vec{k}|^2} \cdot \left(\vec{B}(\vec{k}) \times \vec{B}^*(\vec{k})\right), \qquad (4.3)$$

where $\mathcal{V}$ is the volume of space. Notice that this equality makes use of Maxwell's condition $\vec{\nabla}\vec{B} = 0$, which is ensured by our magnetic field definition (3.7). At our initial time, by virtue of Eqs. (4.1), this quantity is proportional to the winding of the Higgs field. This is defined as the index of the map from the spatial volume to the group SU(2)=S_3, provided by the matrix $\Omega(x)$. A histogram of the winding obtained for our initial Gaussian random field configurations is displayed in Fig. 2. The data are well described by a Gaussian distribution. Since we have not included CP violating terms, the mean value of the winding number is zero. However, we observe a non-zero dispersion from which one can obtain a non-zero volume-independent topological susceptibility $\chi = 0.52 \times 10^{-4}\, m^3$. This translates into a corresponding

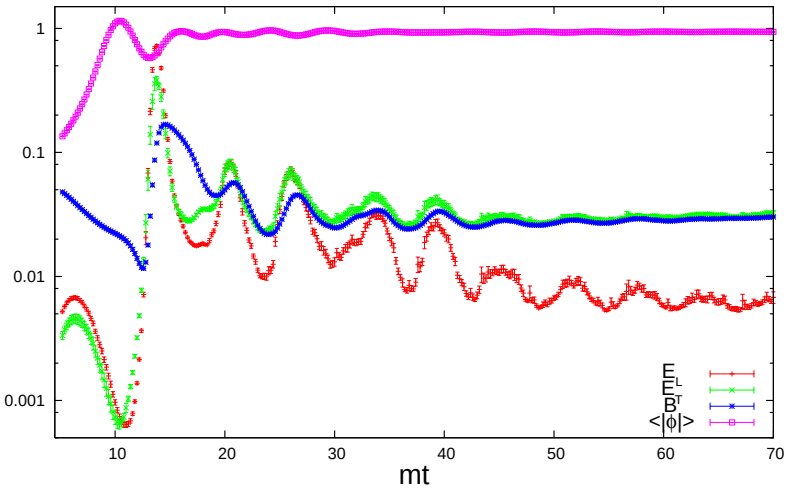

Figure 3: We show the time evolution of the electric (transverse E_T and longitudinal E_L) and magnetic energy densities averaged over 150 configurations for $m_{\rm H} = 3m_{\rm W}$, $ma = 0.42$ and $p_{\rm min} = 0.15\, m$.

non-vanishing helical magnetic susceptibility $\chi_H \equiv \langle H^2 \rangle / \mathcal{V} = 0.38(3)\, m^3$. The Z helical susceptibility at this initial stage is $\chi_Z \equiv \tan^{-4} \theta_W \, \chi_H$.

In the next subsection we will study the evolution of this helical magnetic field during the highly non-linear epoch of symmetry breaking. This provides a connection between magnetic field helicity, Z-strings and the occurrence of configurations carrying non-trivial Chern-Simons number. This result, which relates baryon number generation and magnetic helicity, has been proposed, although along somewhat different lines, by Cornwall [38]. The connection has been studied recently by Copi et al. [83]. They showed that the sphaleron decay indeed gives rise to helical magnetic fields.

At later stages, the Chern-Simons number creation processes stop, leaving behind a remnant magnetic helicity component [36], which is preserved in a plasma with high electrical conductivity. Thus, this could provide a signature of EW generation of primordial magnetic fields.

4.2 Magnetic strings through symmetry breaking

We will now focus upon the evolution of the system from the initial Gaussian random field situation until the onset of symmetry breaking. To have a global picture of the process we show in Fig. 3 the time evolution of the expectation value of the Higgs field from the initial time $mt_i = 5$ of our classical evolution. Notice the strong initial oscillations for times smaller than $mt = 20$, which are then progressively damped at

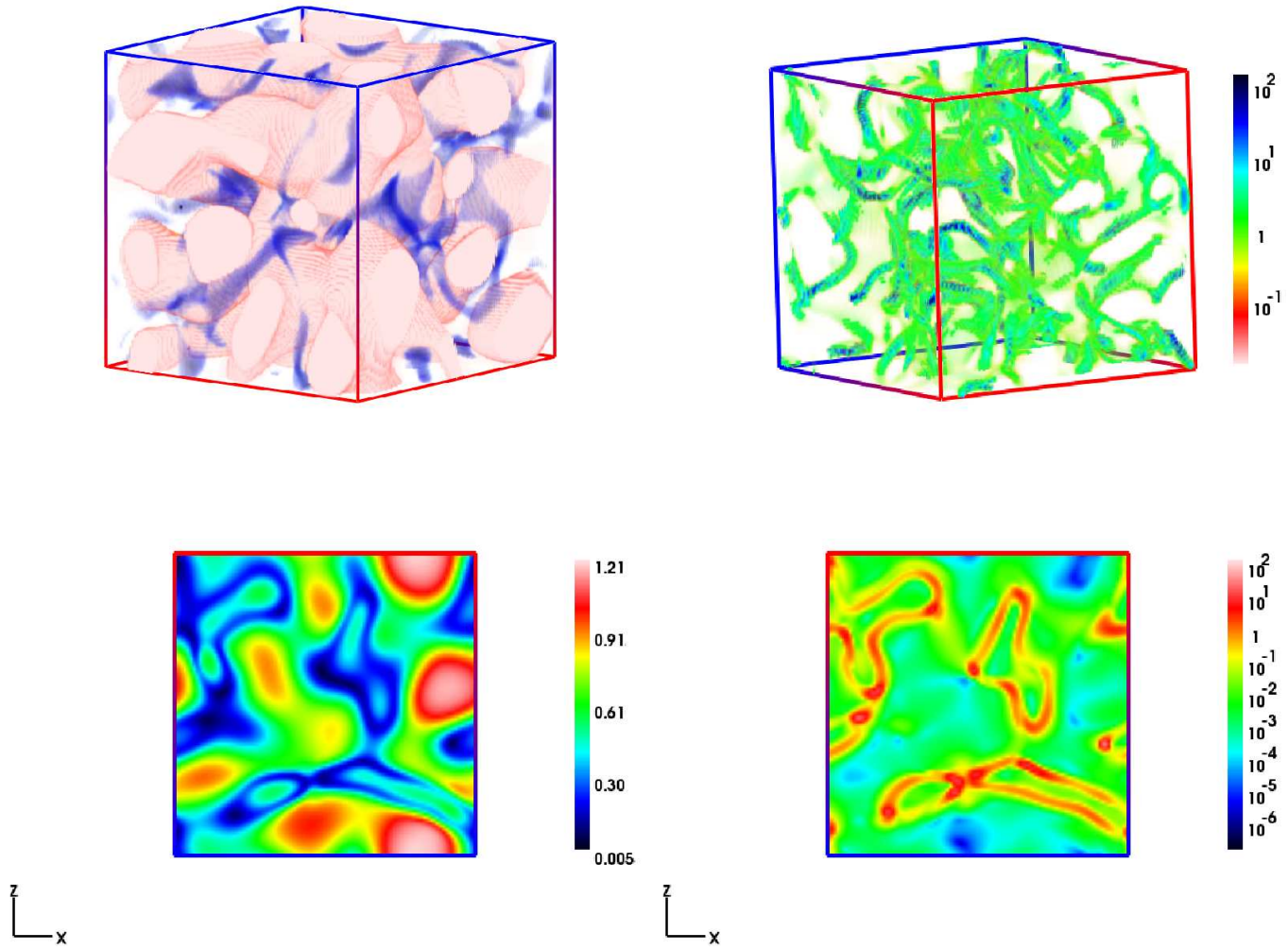

Figure 4: Top: (Left) The location of the bubbles in the Higgs field norm (in red) with a lower cutoff set at $0.7\,v$ and the locus of points with twice the magnetic energy density ($|\vec{B}(\vec{x})|^2$) (in blue) higher than $0.01\,m^4$. (Right) Locus of points where the magnetic energy density is above $0.03\,m^4$. Bottom: (Left) Two-dimensional contour plots of the Higgs field norm. (Right) Two-dimensional contour plots of the magnetic energy density. Data correspond to $mt = 15$ and $m_{\rm H} = 2m_{\rm W}$.

larger times. The figure also displays the fraction of the total energy density carried by electromagnetic fields. We split it into its magnetic and electric components, and for the latter we analyze separately longitudinal and transverse parts. [6] We observe that between $mt = 10$ and $mt = 15$, there is an explosive growth of the electromagnetic fields correlated with the first minimum in the oscillation of the

[6]The technicalities involved in the lattice definition of transverse and longitudinal fields as in the definition of the W bosons charge densities and currents are discussed in Appendix B.

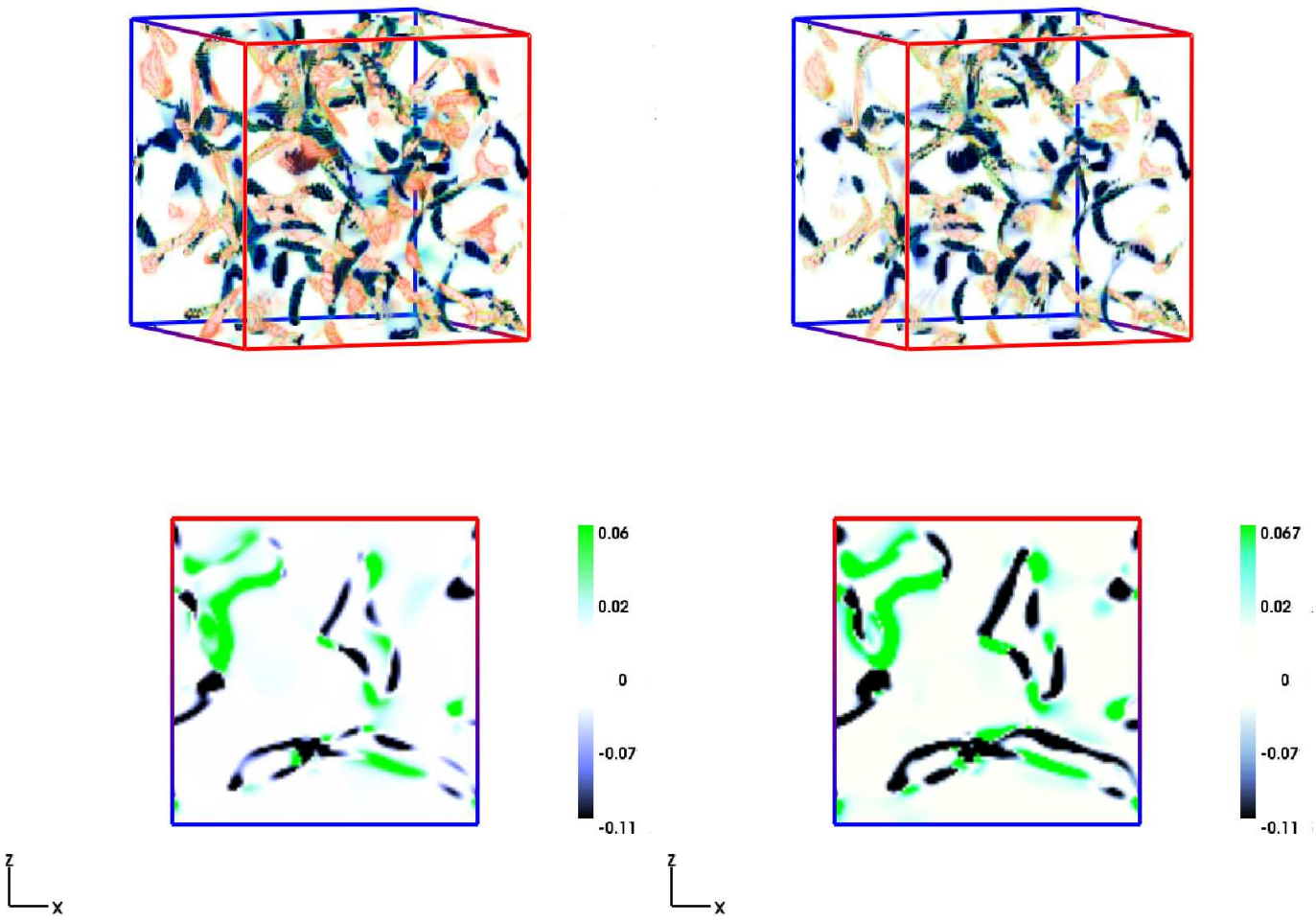

Figure 5: Top: (Left) Helicity of the magnetic field. (Right) Helicity of the Z-boson field. Bottom: (Left) Two dimensional contour plots of the helicity of the magnetic field. (Right) Two dimensional contour plots of the helicity of the Z-boson field. Data correspond to $mt = 15$, for $m_{\rm H} = 2m_{\rm W}$.

Higgs field expectation value. The data in the figure corresponds to $m_{\rm H} = 3m_{\rm W}$, but similar behaviour is observed for the other ratios studied.

We will now present the spatial structure observed for the magnetic fields at $mt = 15$ after the strong oscillation region. The corresponding distribution of the Higgs field modulus has been presented in Ref. [73]. There we showed that the initial Gaussian peaks lead to bubbles which expand and collide with neighbouring ones. This is illustrated in the top left of Fig. 4 where we display a snapshot of the Higgs field norm at $mt = 15$. At this time bubble shells (in red), that have grown out of the peaks in the initial Gaussian random field, fill almost all the volume of the box. Magnetic fields (shown in blue in the figure) appear as string-like structures

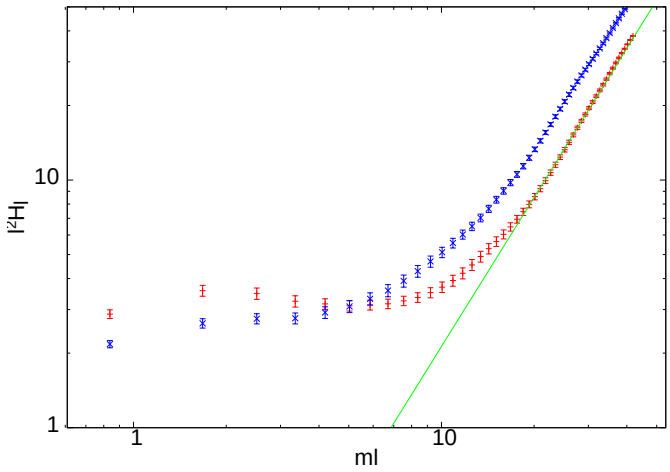

Figure 6: Averaged $l^2 H_l(r_0)$, Eq. (4.4), at $mt = 15$. We also show the l^2 asymptotic behaviour for the $m_{\rm H}/m_{\rm W} = 4.65$ model. The other data corresponds to $m_{\rm H}/m_{\rm W} = 2$.

localized in the region between bubbles, where the Higgs field remains closer to the false vacuum for a longer period of time. This linkage between magnetic strings and Higgs field minima is even more evident in the two dimensional contour plots presented in the bottom half of Fig. 4.

The structures observed in the regions of maximal magnetic density are reproduced when looking at the helical part alone. This is exemplified by the comparison of Fig. 5 with Fig. 4. The figure also shows how the correlation between magnetic and Z boson fields, implicit in our initial conditions, is still preserved once gauge fields and non-linearities have started to play a role. An interesting observation can be made here concerning the connection with baryon number generation. Analysis of the cold EW transition show that sphaleron-like configurations, with non-trivial Chern-Simons number, are also located between bubble shells [74]-[75]. For non-zero Weinberg angle, sphalerons look like magnetic dipoles [84] and it is tempting to correlate the observed helical magnetic flux tubes with the alignment of sphaleron dipoles. Although a detailed investigation of this correlation is beyond the scope of this paper, our results for the distribution of magnetic helicity do indeed hint in that direction. An evaluation of the net helicity at late times and a discussion on its persistence will be postponed to section 5.

In the previous figures, the closed string-like structure of the helicity and magnetic field appears much more clearly that in the Gaussian random field initial condition at $mt_i = 5$. To quantify the string-like character, we have analyzed the following quantity:

$$H_l(r_0) = \frac{1}{l^3} \int_{L(r_0)} dx^3 |\vec{h}(x)| \,, \tag{4.4}$$

where $\vec{h}(x)$ denotes the helicity density and the integration is on a box of length l, centered at a point r_0 at the center of one of the strings. Figure 6 shows the l-dependence of $l^2 H_l(r_0)$, averaged over several configurations. The figure is intended to show the one-dimensional character of the distribution in accordance to our string picture. In that case, $l^2\, H_l(r_0)$ should be l-independent in contrast with the l^2-behaviour characteristic of an isotropic distribution. Both regimes are clearly observed in the figure. The stringy behaviour is displayed up to $ml \sim 10$, beyond which the plot shows how the data tends nicely to a straight line of slope equal to 2. This is to be expected once the box is big enough to contain several strings. This leads to an estimate of the string separation of $m_{\rm H} l \sim 14$, which is a significant fraction of the total length of the box.

4.3 Charge lumps around magnetic field lines

Up to now we have focused on the distribution of magnetic and Z-boson fields, but there is important additional information on the nature of the primordial plasma during these stages of preheating. Note that our initial conditions provide a source for charged W-currents and a non-trivial charge density. It turns out that there is charge separation at the initial stage. Positive and negative charges are clustered into separate lumps which track the magnetic field lines. Figures 7 and 8 show this effect at $mt = 15$ and $mt = 10$, respectively. Note that there is a strong correlation between the magnetic field lines and the distribution of charges of opposite sign around them. The effect is seen particularly clear at early times, $mt = 10$, where the magnetic flux tubes are well defined, and there are fewer of them. The charge separation is consistent with the effect that would be produced by a combination of the drift currents induced by gradient and curvature effects from the magnetic field. The electric field is also strongly correlated with the location of the charge lumps, as expected. This charge separation might be responsible for the very slow screening observed for the longitudinal electric field, which will be discussed in the next section.

The plasma generated during the first stages of evolution is, as we have shown, somewhat different from standard MHD plasmas (composed mainly of protons and electrons, together with photons). Here, long range string-like structures are observed in the electromagnetic fields, and opposite W-charges cluster in large regions of space inducing non-trivial electric fields. It is expected that these charge lumps will eventually disintegrate when the W-fields decay into light fermions (quarks and leptons), which travel at the speed of light and diffuse the charge, leading at late times to a standard MHD plasma.

5. Late time evolution

In order to claim a mechanism for cosmological magnetogenesis, the essential question

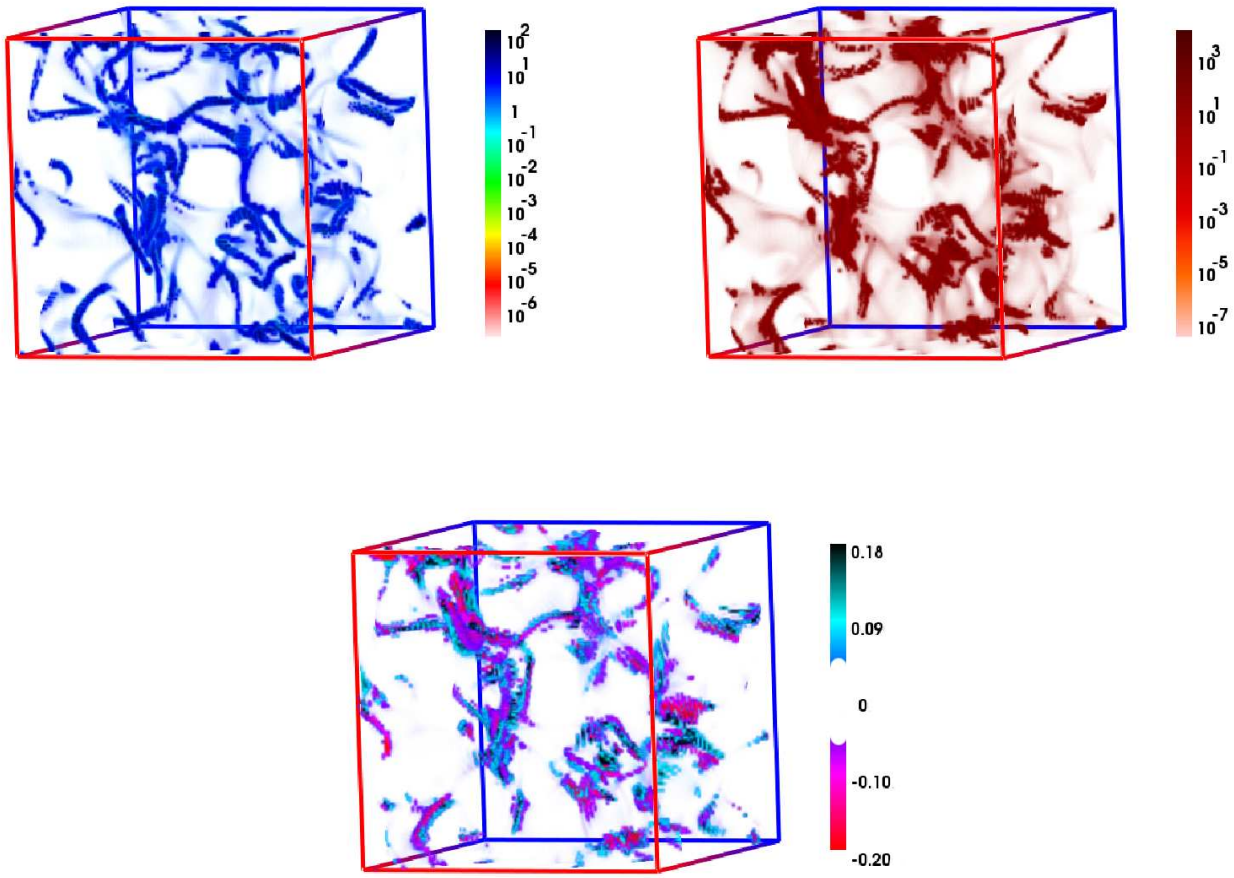

Figure 7: Top Left: Locus of points with magnetic energy density $|\vec{B}(x)|^2$, above $0.01\,m^4$. Top Right: Locus of points with electric energy density $|\vec{E}(x)|^2$ above $0.01\,m^4$. Bottom: The distribution of $W^{\pm}$ charge density, tracking the magnetic field lines. Pink and blue areas represent negative and positive charge densities respectively. Data correspond to $mt = 15$, for $m_{\rm H} = 2m_{\rm W}$.

is whether the amplitude and correlation length of the generated fields are enough to seed the large scale magnetic fields observed today. In this section we will present evidence that a significant fraction of long range helical magnetic fields remains after EW symmetry breaking and is even amplified at later times, a period in which kinetic turbulence has been observed [85, 79]. As we will see below, our estimate for the amplitude of the magnetic field seed gives a fraction $\sim 10^{-2}$ of the total energy density at the EW scale. This could be enough to seed the cluster and supercluster values without the need for a dynamo mechanism.

More difficult is to address the issue of whether the magnetic field spectrum experiences inverse cascade, i.e. transference of energy from high to low momentum

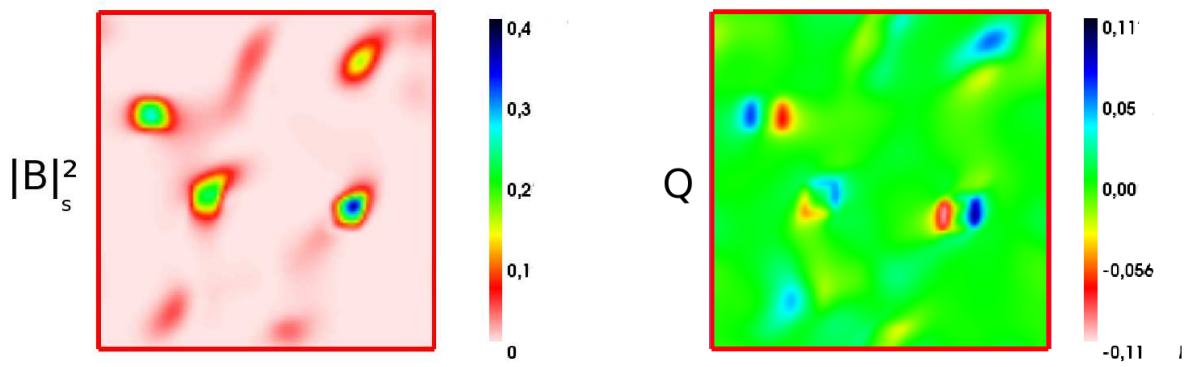

Figure 8: Left: Locus of points with magnetic field density $|\vec{B}(\vec{x})|^2$ above $0.01\, m^4$. Right: The 2-dimensional W-charge distribution localized in lumps of opposite sign facing each other. Note that the location of the charge lumps is strongly correlated with the magnetic field flux tubes. These figures correspond to early times, $mt = 10$, for $m_{\rm H} = 3m_{\rm W}$.

modes [29]-[33]. Inverse cascade is required to make the coherence length of the magnetic field grow (almost) as fast as the horizon until the time of photon decoupling. Our approach does not allow to extrapolate the time evolution for sufficiently long times. Nevertheless, we will provide some evidence that inverse cascade might be at work. However, additional work is required to analyze if it can be sustained for a sufficiently long time. This might require a full magnetohydrodynamics treatment of the time evolution for which our set up will provide an initial condition.

5.1 Magnetic helicity and electromagnetic energy densities

We will first analyze in detail how electromagnetic fields evolve in time, paying particular attention to the evolution of the magnetic field helicity long after SSB.

As mentioned above, the relevant quantity for helicity in the absence of CP violation is the helical susceptibility χ_H. Its time evolution, for different values of the $m_{\rm H}/m_{\rm W}$ ratio, is displayed in Fig. 9. At the same time we display the helical susceptibility of the Z boson magnetic field, rescaled by $\tan^4\theta_W$ to make it agree with the initial electromagnetic helicity, see discussion after Eq. (4.3). The late time behaviour, after $mt \sim 60$, gives further support to the Vachaspati-Cornwall's conjecture. It corroborates that, while the Z boson helicity is damped in time, the magnetic helicity is preserved and even increases with a power law dependence in time given by t^α with $\alpha = 0.7(1), 0.8(1), 0.3(1)$ for $m_{\rm H}/m_{\rm W} = 2, 3$ and 4.65 respectively. The corresponding helical susceptibilities at $mt = 100$ are $0.11(2), 0.26(1), 0.12(2)\ m^3$. Note that the model with $m_{\rm H} = 3m_{\rm W}$ is more efficient than the others in generating

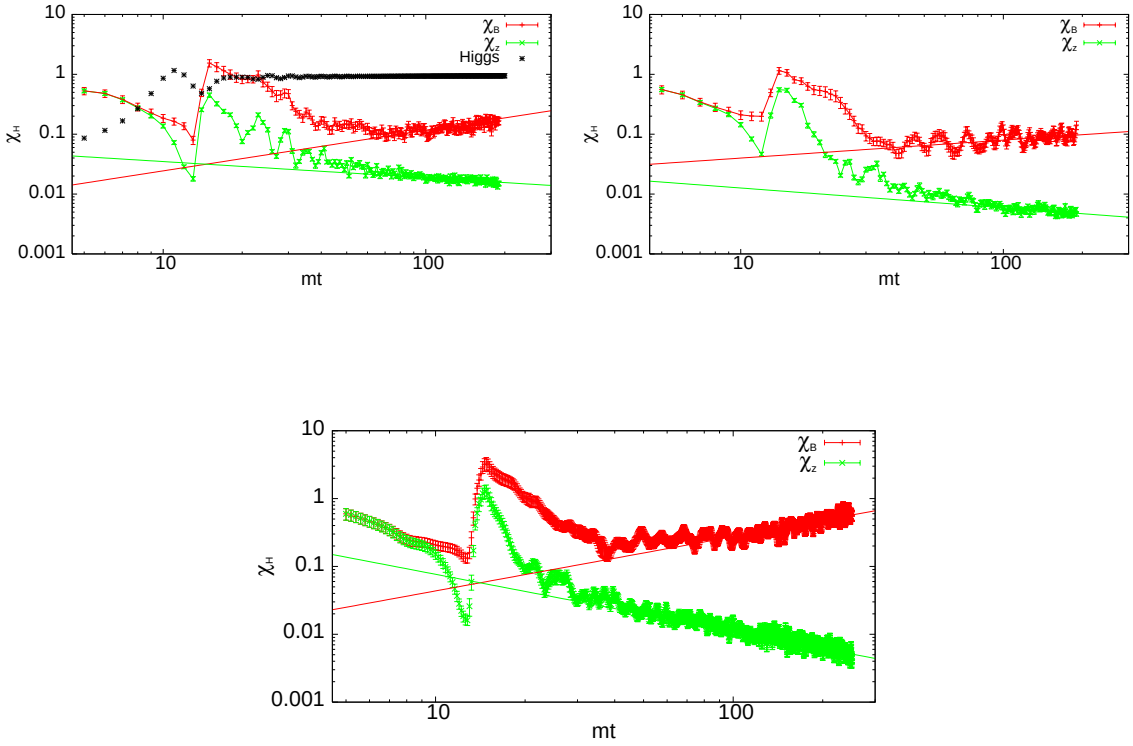

Figure 9: We display the time evolution of the helical susceptibilities for the magnetic field (with fit t^α) and the Z-boson field (with fit t^β). The latter is rescaled by $\tan^4\theta_W$ to match the initial electromagnetic helicity. Top left is for $m_{\rm H}/m_{\rm W} = 2$, averaged over 80 configurations, with $\alpha = 0.7(1)$ and $\beta = -0.27(4)$. Top right is for $m_{\rm H}/m_{\rm W} = 4.65$, averaged over 80 configurations, with $\alpha = 0.3(1)$ and $\beta = -0.33(5)$. Bottom is for $m_{\rm H}/m_{\rm W} = 3$, averaged over 200 configurations, with $\alpha = 0.8(1)$ and $\beta = -0.82(4)$. All data correspond to $ma = 0.42$ and $p_{\rm min} = 0.15\,m$. The top left figure also shows the time evolution of the Higgs mean to illustrate the time when SSB takes place.

helicity at late times. This suggests a non monotonic dependence of the helicity on the Higgs to W mass ratio, a feature also observed in the generation of Chern-Simons number [75, 74]. In the remaining of this section we will focus on results for this particular value of the mass ratio. Comments upon the dependence on $m_{\rm H}/m_{\rm W}$ are deferred to section 6.2.

The late time evolution of the integrated magnetic, longitudinal and transverse electric energies, for $m_{\rm H} = 3m_{\rm W}$ is presented in Fig. 10. A large fraction of the electromagnetic fields generated after SSB is preserved by the time evolution. From $mt \sim 60$ onwards, the transverse energy densities increase with time, again with a power law dependence: t^α, with $\alpha = 0.350(1)$ and $0.330(1)$ for electric and magnetic

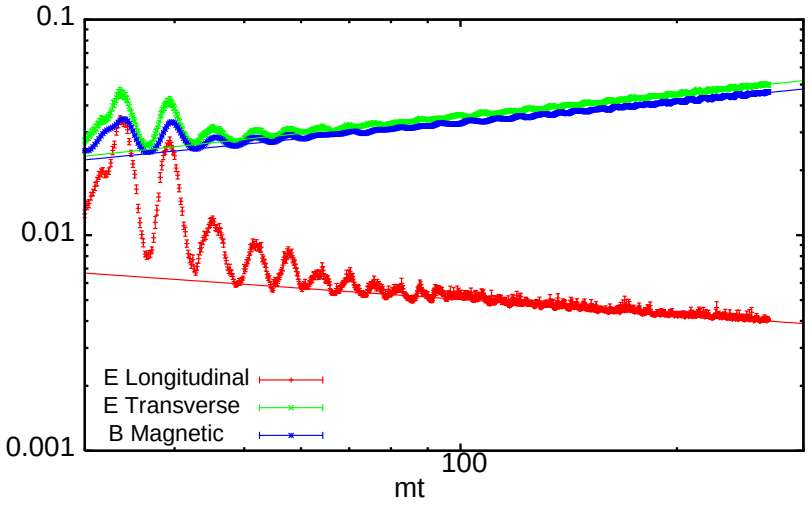

Figure 10: We display the log-log plot of the time evolution of the electric (transverse and longitudinal) and magnetic energy densities. The exponents of the power law fits are: Transverse electric field: 0.350(1); Magnetic field: 0.330(1) and Longitudinal electric field: $-0.234(2)$. For $m_{\rm H} = 3\, m_{\rm W}$, $ma = 0.42$ and $p_{\rm min} = 0.15\, m$, averaged over 200 configurations.

energy densities respectively. At these late times, transverse electromagnetic fields are composed of an admixture of radiation and long range seed fields. In section 5.2 we will see how to separate these two components by analyzing the electromagnetic field power spectra. Note also that there is a significant fraction of longitudinal electric fields, even at the later stages of the evolution. As already mentioned, the slow screening of the longitudinal component of the electric field is tied to the presence of large charged lumps around magnetic field lines, see Figs. 7 and 8, which persist even at late times.

5.2 Electromagnetic field spectrum

To investigate whether inverse cascade is active during the late time evolution we have analyzed the electromagnetic Fourier spectrum. Figs. 11 and 12 display the time evolution of $\langle k^2 |\vec{E}(k)|^2\rangle/\mathcal{V}$ and $\langle k^2 |\vec{B}(k)|^2\rangle/\mathcal{V}$, where $\vec{E}(k)$ and $\vec{B}(k)$ are the Fourier components of the electromagnetic fields and $\mathcal{V}$ is the physical volume. The most remarkable feature in the spectrum is the peak at small momenta that develops with time, which is distinctly separated from the high momentum component. This behaviour suggests that the spectrum contains two uncorrelated distributions which describe respectively electromagnetic radiation and the long range electric and magnetic seed fields. Following this indication, we have performed fits to the spectrum

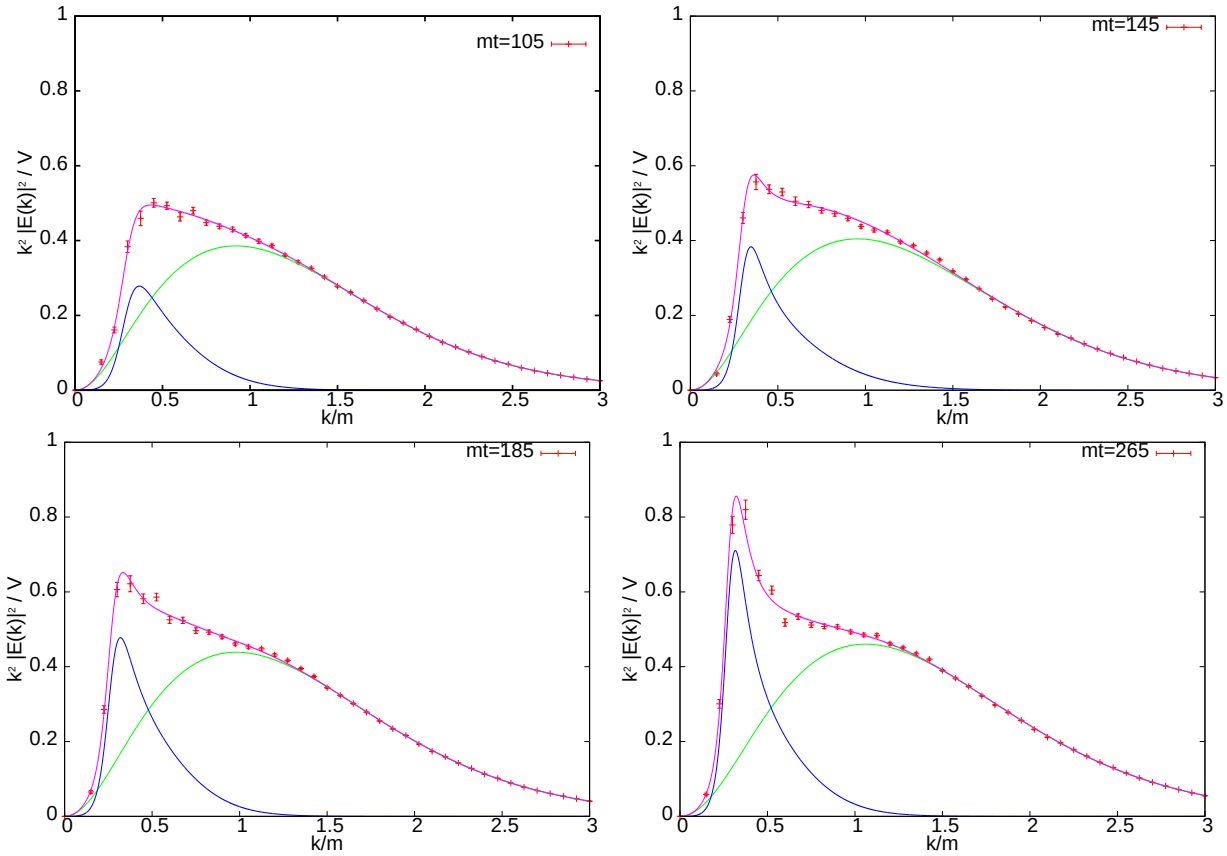

Figure 11: We plot $\langle k^2|\vec{E}(k)|^2\rangle/\mathcal{V}$ vs k, averaged over 150 configurations. The lines represent fits to the radiation and seed field electromagnetic components according to Eqs. (5.3), (5.5) respectively. Results are presented at $mt = 105$, 145, 185 and 265. In all cases $m_{\rm H} = 3m_{\rm W}$, $ma = 0.42$ and $p_{\rm min} = 0.15\, m$.

where this separation is made explicit:

$$\vec{F}(k) = \vec{F}^{\rm seed}(k) + \vec{F}^{\rm rad}(k) \tag{5.1}$$

with $\vec{F} = \vec{E}$ or $\vec{B}$. For the expectation values of the electric and magnetic correlators we obtain accordingly:

$$\begin{aligned} \langle|\vec{E}(k)|^2\rangle &= \langle|\vec{E}^{\rm seed}(k)|^2\rangle + \langle|\vec{E}^{\rm rad}(k)|^2\rangle \\ \langle|\vec{B}(k)|^2\rangle &= \langle|\vec{B}^{\rm seed}(k)|^2\rangle + \langle|\vec{B}^{\rm rad}(k)|^2\rangle \end{aligned} \tag{5.2}$$

In the remaining of this section we will describe these two components, starting with the electromagnetic radiation and ending with the infrared component which describes the magnetic field seed.

5.2.1 Electromagnetic radiation

The radiation component dominates the electromagnetic energy density, its contri-

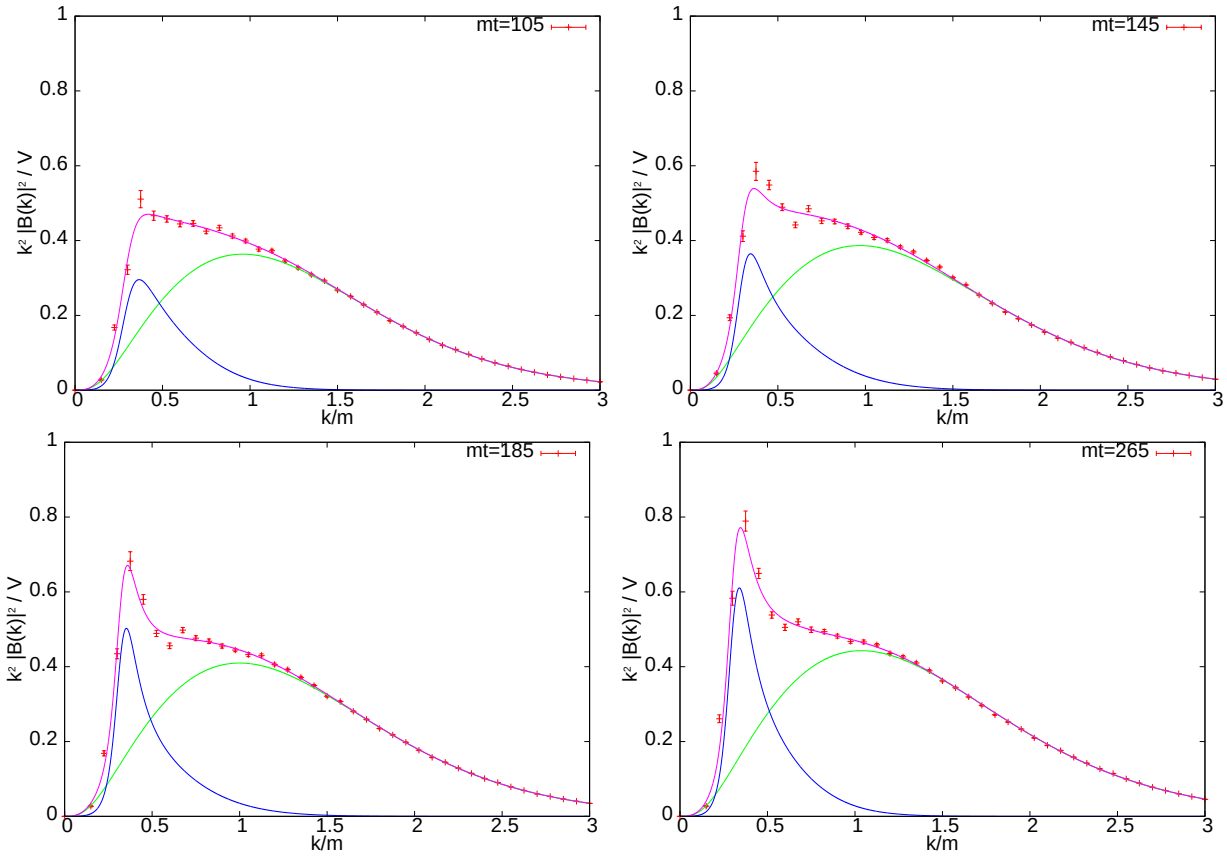

Figure 12: The same as in Fig. 11 but for the magnetic component: $\langle k^2|\vec{B}(k)|^2\rangle/\mathcal{V}$.

bution being a factor of 5-10 larger than the one coming from seed fields. Its profile is very well described by:

$$\begin{aligned}\frac{1}{\mathcal{V}}\langle|\vec{E}^{\rm rad}(k)|^2\rangle &= \frac{2w_E}{e^{\beta(w_E-\mu_E)}-1}\\ \frac{1}{\mathcal{V}}\langle|\vec{B}^{\rm rad}(k)|^2\rangle &= \frac{2k}{e^{\beta(w_B-\mu_B)}-1}\,,\end{aligned} \tag{5.3}$$

with $w_{E(B)}=\sqrt{k^2+m^2_{E(B)}}$ and parameters given in Table 2. As illustrated in figures 11 and 12, this distribution fits very well the high momentum part of the spectrum but fails in reproducing the low momentum peak. Eq. (5.3) represents free massive thermal radiation with non zero chemical potential at temperatures slightly rising with time, which we interpret as an effect induced by the plasma of the W-fields.

Similar information can be extracted from the distribution of local values of the norm of the transverse electric and magnetic fields. For free photons this should follow a Maxwellian distribution (see Appendix C):

$$P(B)=\sqrt{\frac{2}{\pi}}\Big(\frac{3}{\langle B^2\rangle}\Big)^{3/2}B^2\;e^{-\frac{3B^2}{2\langle B^2\rangle}}, \qquad . \tag{5.4}$$

mt	T_E/m	m_E/m	μ_E/m	T_B/m	m_B/m	μ_B/m
105	0.32(1)	0.77(1)	0.61(1)	0.32(1)	0.66(1)	0.60(1)
125	0.33(1)	0.74(1)	0.58(1)	0.33(1)	0.61(2)	0.57(2)
145	0.34(1)	0.75(1)	0.58(1)	0.33(1)	0.60(2)	0.56(2)
165	0.34(1)	0.76(2)	0.59(1)	0.34(1)	0.61(2)	0.57(2)
185	0.34(1)	0.82(1)	0.63(1)	0.34(1)	0.65(2)	0.60(2)
205	0.35(1)	0.84(1)	0.64(1)	0.34(1)	0.64(2)	0.59(2)
245	0.35(1)	0.93(1)	0.68(1)	0.35(1)	0.64(1)	0.59(2)
265	0.36(1)	0.93(1)	0.67(1)	0.35(1)	0.65(2)	0.59(2)

Table 2: Parameters of the fit to the high momentum part of the transverse electric and magnetic spectra in Eq. (5.3), for $m_{\rm H} = 3m_{\rm W}$, $ma = 0.42$ and $p_{\rm min} = 0.15\, m$. Errors in parenthesis combine both systematic and statistical effects.

where $B = |\vec{B}(\vec{x})|$. Our data does indeed reproduce this behaviour at late times. In Fig. 13 we display the time evolution of the distribution of magnetic field norms, starting from $mt = 5$. Although initially the distribution differs significantly from the Maxwellian one, it is approached as time evolves and photons thermalise. There is, however, a systematic mismatch when we fit the tail of the Maxwellian distribution, even at large values of mt. This signals again a deviation from free radiation, like the one observed in the low momentum part of the magnetic and electric spectra. It is in this deviation where the contribution of the seed magnetic fields reside.

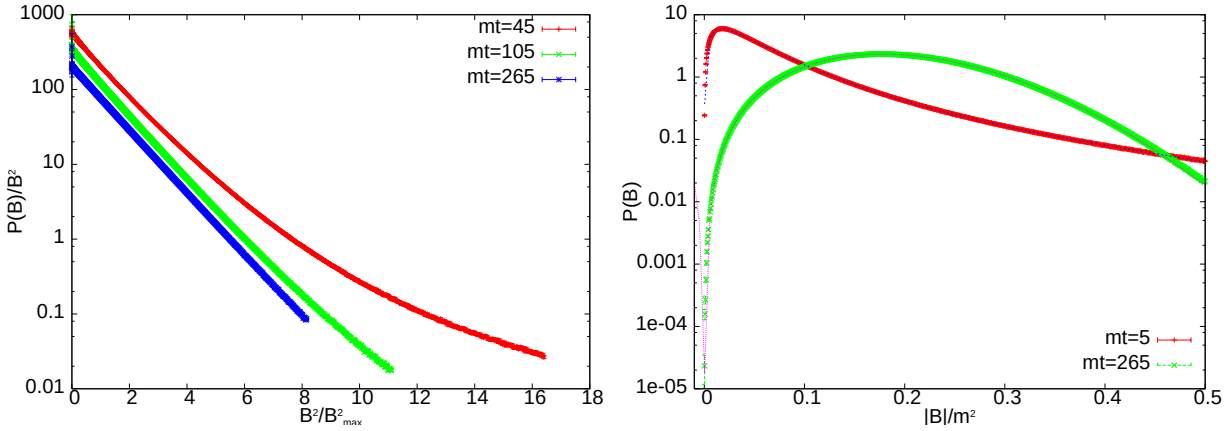

Figure 13: We show the time evolution of the distribution of magnetic field norms. Left: For $m_{\rm H} = 3m_{\rm W}$ we display the log of $P(B)/B^2$ vs $B^2/B^2_{\rm max}$ (i.e. normalized to the value at the peak of the distribution) . Right: For $m_{\rm H} = 3m_{\rm W}$ we compare the initial distribution of the local magnitude of the magnetic field at $mt = 5$ with the one obtained at $mt = 265$, the latter fitted to a Maxwellian distribution. The fit to the $mt = 5$ data is described in Appendix D.

5.2.2 Electric and magnetic seeds

We turn now to the analysis of the infrared part of the spectrum, which is the relevant one for the generation of the LSMF seed field. This low momentum part has been fitted to:

$$\frac{1}{\mathcal{V}}\langle|\vec{E}^{\rm seed}(k)|^2\rangle = \frac{2k}{e^{\hat{\beta}_E(\hat{w}_E-\hat{\mu}_E)}-1}\,, \qquad \frac{1}{\mathcal{V}}\langle|\vec{B}^{\rm seed}(k)|^2\rangle = \frac{2k}{e^{\hat{\beta}_B(\hat{w}_B-\hat{\mu}_B)}-1}\,, \tag{5.5}$$

with $\hat{w}_{E(B)} = \sqrt{(k-k^0_{E(B)})^2+\hat{m}^2_{E(B)}}$ and parameters given in Tables 3, 4. This could represent again massive radiation at non-zero chemical potential if it were not for the peculiar shift k_0 in the frequency $\hat{w}$. We interpret the value of $k_0 \sim 0.3m$ as a characteristic momentum scale of the long range electromagnetic fields.

mt	$\hat{T}_E/m$	$\hat{m}_E/m$	$\hat{\mu}_E/m$	$\hat{k}^0_E/m$
105	0.11(1)	0.33(5)	0.30 (4)	0.29(1)
125	0.13(1)	0.24(4)	0.22(3)	0.29(1)
145	0.14(1)	0.21(5)	0.18(3)	0.30(1)
165	0.13(1)	0.25(5)	0.23(3)	0.29(1)
185	0.09(2)	0.49(8)	0.48(6)	0.27(1)
205	0.11(1)	0.36(6)	0.35(3)	0.29(1)
225	0.10(2)	0.39(10)	0.38(3)	0.28(1)
245	0.11(1)	0.37(7)	0.35(3)	0.30(1)
265	0.10(1)	0.45(7)	0.44(4)	0.28(1)

Table 3: Parameters of the fit to the low momentum part of the transverse electric spectrum in Eq. (5.5), for $m_{\rm H} = 3m_{\rm W}$, $ma = 0.42$ and $p_{\rm min} = 0.15\,m$.

A quantitative estimate of the energy density and correlation length of the seed electromagnetic fields can be obtained from our fits to the low momentum part of the spectrum. The mean energy density is computed from the integral of the seed field spectrum as

$$\langle\rho^F_{\rm seed}\rangle = \frac{1}{2\mathcal{V}}\sum_{\vec{k}}\frac{|\vec{F}^{\rm seed}(k)|^2}{\mathcal{V}}\,, \tag{5.6}$$

with $F = E(B)$. The correlation length, $\xi_{E(B)}$, is extracted from

$$\xi = \frac{2\pi}{\bar{k}}\ ,\ \text{with}\ \bar{k}^2 = \frac{\sum_{\vec{k}} k^2\ |\vec{F}^{\rm seed}(k)|^2}{\sum_{\vec{k}}|\vec{F}^{\rm seed}(k)|^2}\,. \tag{5.7}$$

Table 5 and Fig. 14 summarise our results. We have tested finite volume independence by comparing two different physical volumes: $p_{\rm min} = 0.125\,m$ and $p_{\rm min} = 0.15\,m$.

mt	$\hat{T}_B/m$	$\hat{m}_B/m$	$\hat{\mu}_B/m$	$\hat{k}_B^0/m$
105	0.11(1)	0.32(7)	0.30(3)	0.29(1)
125	0.13(1)	0.24(7)	0.21(4)	0.31(1)
145	0.13(1)	0.24(6)	0.22(3)	0.29(1)
165	0.13(1)	0.27(6)	0.23(4)	0.29(1)
185	0.13(2)	0.18(10)	0.16(8)	0.32(3)
205	0.11(1)	0.31(7)	0.29(4)	0.30(1)
225	0.11(1)	0.26(5)	0.25(4)	0.31(1)
245	0.10(1)	0.37(9)	0.36(2)	0.29(1)
265	0.11(2)	0.33(9)	0.32(3)	0.30(1)

Table 4: Parameters of the fit to the low momentum part of the magnetic spectrum in Eq. (5.5). For $m_{\rm H} = 3m_{\rm W}$, $ma = 0.42$ and $p_{\rm min} = 0.15\,m$.

The numbers in Table 5 come from an average of the results obtained at these two physical volumes, with errors given by the dispersion between them.

We obtain a magnetic seed whose mean energy density increases linearly with time. Within the time ranges we have analysed, its fraction to the total comes out to be of order $\sim 10^{-2}$. Assuming the magnetic field expands as radiation, this would give magnetic fields today of order $0.5\,\mu G$, which are in the range of the observed ones in galaxies, and even in clusters of galaxies, where no-extra amplification through a dynamo mechanisms is expected.

mt	$\langle\rho^E_{\rm seed}\rangle(\times 10^2)$	$m\xi_E$	$\langle\rho^B_{\rm seed}\rangle(\times 10^2)$	$m\xi_B$
105	0.62(5)	25.3(1)	0.58(3)	25.7(6)
125	0.73(2)	25.2(1)	0.61(1)	24.5(9)
145	0.76(4)	24.8(9)	0.72(2)	24.8(3)
165	0.76(4)	26.0(10)	0.77(1)	25.4(6)
185	0.83(1)	27.6(1)	0.79(2)	26.0(10)
205	0.89(2)	27.7(2)	0.79(6)	27.2(5)
225	0.91(5)	27.9(5)	0.87(1)	28.0(5)
245	1.06(9)	27.6(4)	0.88(1)	28.1(2)
265	1.12(7)	27.9(2)	0.92(2)	28.4(7)

Table 5: Fraction of total energy and correlation length of the seed electromagnetic fields. They are both derived from the infrared spectrum as described in Eqs. (5.6) and (5.7). The results are obtained by averaging (over 150 configurations) the values obtained for $p_{\rm min} = 0.15\,m$ and $p_{\rm min} = 0.125\,m$, with errors reflecting the dispersion between them. Data correspond to $m_{\rm H} = 3m_{\rm W}$, $ma = 0.42$.

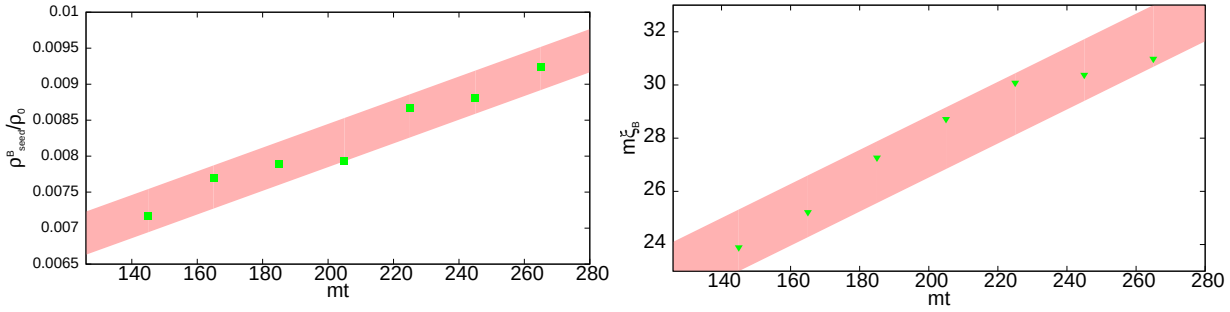

Figure 14: We show the time evolution of $\rho^B_{\rm seed}$ (left) and $m\xi_B$ (right), for $m_{\rm H} = 3m_{\rm W}$, $ma = 0.42$. The results are obtained by averaging the values obtained for $p_{\rm min} = 0.15\,m$ and $p_{\rm min} = 0.125\,m$, with bands representing the dispersion in the errors. The fits are $\rho^B_{\rm seed}/\rho_0 = 0.0035(5) + 2.3(3) \times 10^{-5} mt$ and $m\xi_B = 20.1(4) + 0.033(2)mt$ respectively.

Concerning the correlation length, it is difficult to make a definitive statement about the presence of inverse cascade, given the small time scales we can explore with our numerical simulation. Nevertheless, within the time span we have analyzed, our results clearly show a linear increase of the magnetic correlation length with time (see Fig. 14). This result is robust under changes of $p_{\rm min}$ and lattice spacing. The observed growth is described by $m\xi_B(t) = 20.1(4) + 0.033(2)mt$, giving at $mt = 265$ a characteristic length scale for seed magnetic fields of order $m\xi_B(mt = 265) \sim 30(1)$. This is much larger than the thermal correlation length, $m\xi_{\rm thermal} \sim 10$, and represents a significant fraction of the physical volume. It also implies a considerable increase from the initial value at $mt = 5$, obtained from the initial spectrum to be $m\xi_B(mt = 5) \sim 17$. From these results we can safely conclude that the time evolution has succeeded in amplifying the correlation length of the magnetic seed generated at SSB. Nevertheless, a more detailed study, including plasma effects, would be required to determine whether ξ will be further amplified at late times.

In addition to the direct analysis of the spectrum we have also followed an alternative strategy to separate both the magnitude and the scale of the magnetic remnant from the radiation bath. A common way to do this, which has been extensively used in the literature, is through the computation of several spatial averages of the electromagnetic fields. Following Ref. [28], we introduce the following averages:

- A line average:

$$B_{(1)}(l) = \frac{1}{l} \int_C \vec{B} \cdot d\vec{x}\,, \tag{5.8}$$

  with C a straight line of length l.

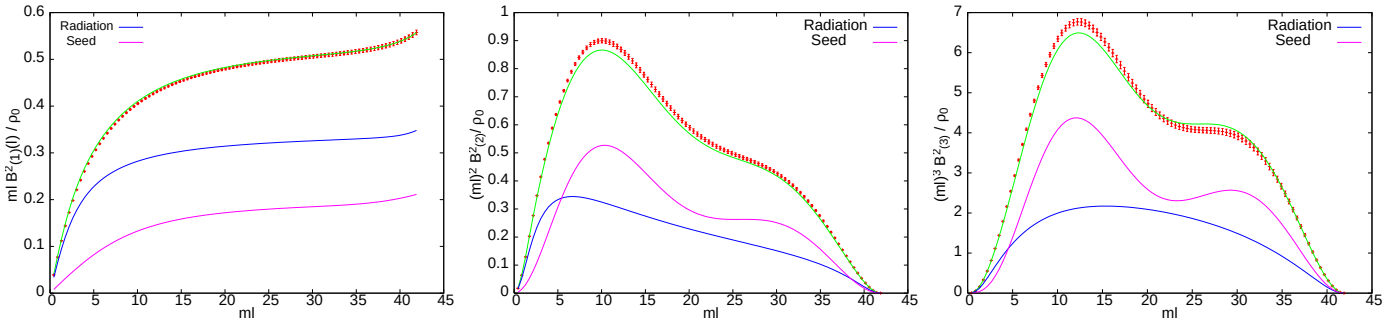

Figure 15: We show the dependence with ml of the three spatial averages (5.8)−(5.10), for $mt = 245$. The lines are extracted from our fits to the infrared and radiation parts of the spectrum. Note that the fall-off at large distances is just a volume effect.

- The average magnetic flux over a surface of area l^2:

$$B_{(2)}(l) = \frac{1}{l^2}\int_S \vec{B}\cdot d\vec{S}\,, \tag{5.9}$$

- A volume average:

$$\vec{B}_{(3)}(l) = \frac{1}{l^3}\int_S \vec{B} d^3x\,. \tag{5.10}$$

As discussed in Ref. [28], the spatial and statistical averages $\langle B^2_{(i)}(l)\rangle$ can be easily computed in terms of the spectra of the fields. For instance, the line average for a volume $\mathcal{V}$ is given by:

$$\langle B^2_{(1)}(l)\rangle = \frac{1}{\mathcal{V}}\sum_{\vec{k}}\frac{|B_k|^2}{\mathcal{V}}W^2(k_1,l) \tag{5.11}$$

with

$$W(k_i,l) = \frac{2\sin(k_i l/2)}{k_i l}. \tag{5.12}$$

Analogous expressions can be found for the other two quantities. The advantage of these averages is that they filter out the high momentum part of the spectrum and allow to recover, at large l, information about the low momentum modes. We have checked that our fits to the spectrum correctly reproduce the spatial averages. This is illustrated in Fig. 15, where we present results for the three averages at $mt = 245$ compared with the predictions obtained from our fits to the spectrum. The quality of the agreement can be considered very good given that the continuum lines are directly obtained from the fits to the spectrum (Eqs. (5.3), (5.5) and Tables 2 - 4), and not as a result of a fit to the spatial averages.

To summarize, we have found evidence of the presence of a long range helical magnetic field, whose amplitude and correlation length are linearly increasing with

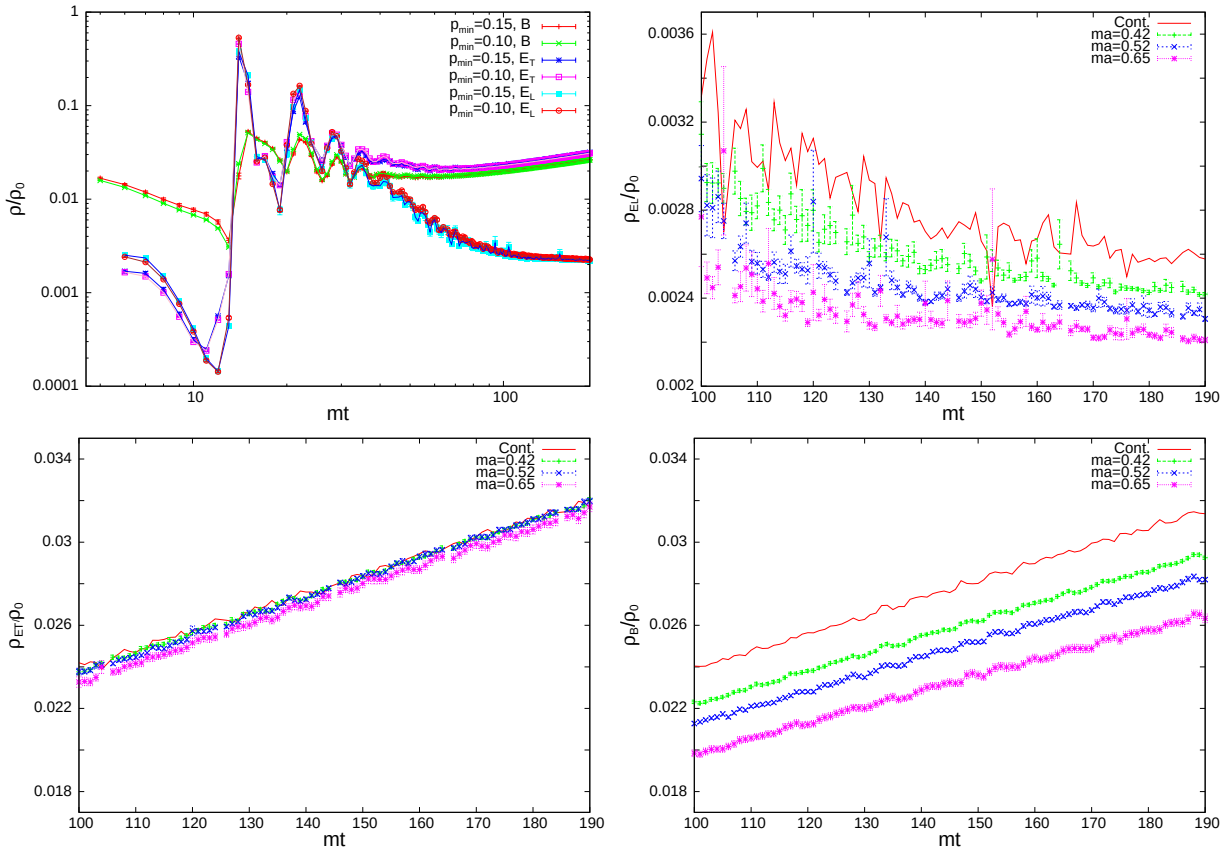

Figure 16: Comparison of the fraction of total energy carried by electric (transverse and longitudinal) and magnetic fields. Top left: for two different values of the minimum momentum: $p_{\rm min} = 0.1$ and 0.15 for fixed $ma = 0.65$. Top Right and down: 3 different lattice spacings ma= 0.65, 0.52,0.42, for the longitudinal, transverse and magnetic components of the energy. The lines are the extrapolation of the results to the continuum $a \to 0$ limit. For $m_{\rm H} = 2m_{\rm W}$ which, from the point of view of lattice artefacts, is the worst case situation.

time. This is accompanied by the growth of a similar long range electric field. The fate of these electromagnetic field depends on the subsequent evolution of the plasma which is not addressable within our classical approximation and would require a magnetohydrodynamics treatment including the effects of fermion fields. Our results for the power spectrum of the seed fields can be used as initial conditions for a MHD treatment as the one developed in Ref. [31].

6. Dependence on methodological and model parameters

In this section we study the (in-)sensitivity of our results to the lattice and finite volume artefacts. We conclude that all our qualitative results are unaffected by both types of approximations. Furthermore, we estimate the size of the systematic errors

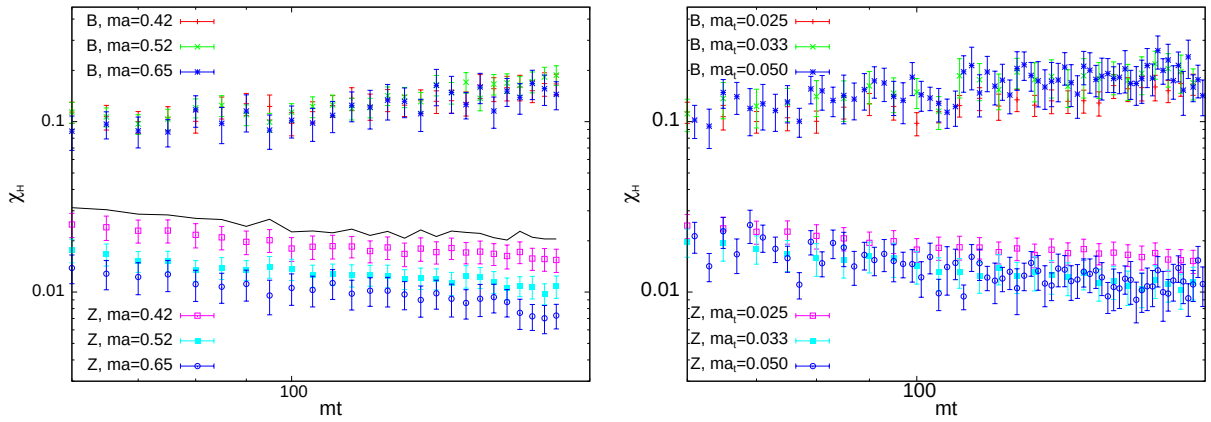

Figure 17: Left: Lattice spacing dependence of the magnetic susceptibility for $m_H = 2m_W, ma = 0.65,\, 0,52,\, 0.42$ and $N = 64,\, 80,\, 100$. Right: Temporal lattice spacing dependence of the magnetic susceptibility for $ma_t = 0.05, 0.025$.

induced by these cut-offs. The lattice artefacts, though sizable, follow the expected $\mathcal{O}(a^2)$ dependence allowing an extrapolation of the most relevant quantities to the continuum limit.

We also analyze the dependence of our magnetic field production mechanism on the Higgs to W-boson mass ratio $m_{\rm H}/m_{\rm W}$. It follows from our scenario that, initially, the helical susceptibility χ_H is independent of the Higgs self-coupling. At later times however, we observe a non-monotonic dependence upon the mass ratio, which is maximal at our intermediate value $m_{\rm H}/m_{\rm W} = 3$.

6.1 Lattice and finite volume artefacts

In order to determine the size of the errors introduced by our numerical approach, we have performed simulations at different values of the physical volume and of the spatial and temporal lattice spacings. The list of simulation parameters is given in Table 1. The selection of values implies a delicate compromise among different factors. As shown in Ref. [73], to avoid important finite volume effects, we need lattices with momentum discretization $p_{\rm min} = 2\pi/L \leq 0.15\, m$. On the other hand, concerning lattice artefacts, we have seen in Ref. [74] that cut-off independence of certain particular quantities (as the Chern-Simons number) requires $m_{\rm W} a \leq 0.3$. Most of our lattices satisfy both requirements.

In Figs. 16 and 17 we present results exhibiting the lattice and finite volume dependence of the electromagnetic energy densities and of the magnetic helicity. They correspond to the most disfavourable case of $m_{\rm H} = 2m_{\rm W}$. No noticeable dependence on the volume is appreciated. Lattice spacing artefacts are somewhat stronger but do not change the general pattern of behaviour. To analyse this effect in more detail, we display in Fig. 18 the a^2 dependence of the electromagnetic field energy densities

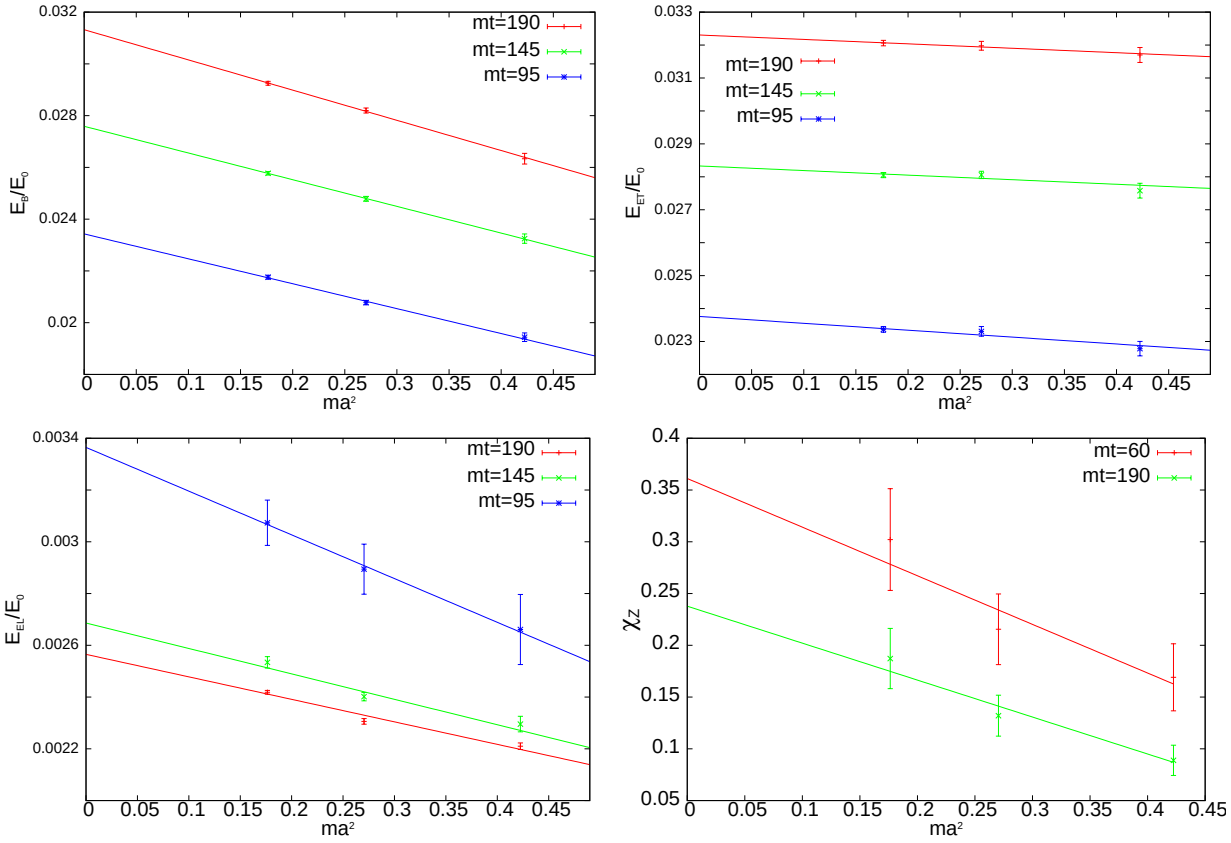

Figure 18: Continuum extrapolation of the magnetic, transverse electric, longitudinal electric and Z-boson susceptibility. For $m_{\rm H} = 2m_{\rm W}$ and $mt = 95$, 145, 190, and $mt = 60$, 190 for the susceptibility.

and Z-boson susceptibility at various times. In all cases the results are consistent with the expected quadratic dependence. This allows the extrapolation of the results to the continuum limit, displayed as a continuous line in Figs. 16 and 17. The right-hand side of the last figure shows that for the case of the magnetic susceptibility the values obtained for the different lattice spacings are compatible within statistical errors. Nonetheless, assuming that the lattice spacing dependence depends smoothly on time, we can obtain an extrapolation to the continuum limit lying approximately 5% above the values obtained for the smaller spacing.

With respect to finite size effects, long range quantities are expected to be the most affected. Thus, it is essential to test that the low momentum part of the magnetic power spectrum is not biased by finite volume artefacts. In Fig. 19 we present results for $p_{\rm min} = 0.125\,m$ and $0.15\,m$. The agreement is very good for the ratio $m_{\rm H}/m_{\rm W} = 3$ and preserves the same quality for the other 2 values of the $m_{\rm H}$ to $m_{\rm W}$ mass ratios that we have studied.

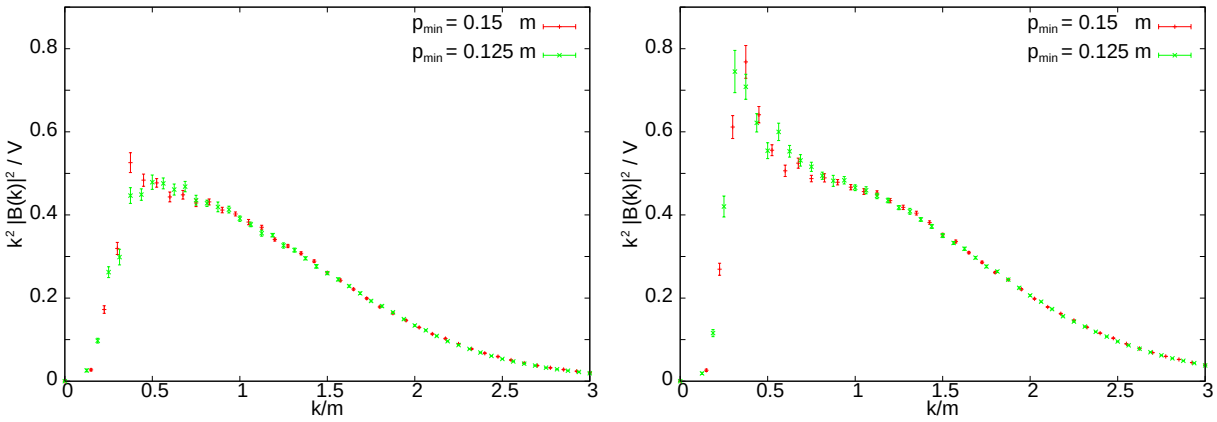

Figure 19: We plot $\langle k^2|B(k)|^2\rangle/\mathcal{V}$ vs k for the magnetic component of the electromagnetic energy. A comparison is made between results at $p_{\rm min} = 0.125\,m$ and $p_{\rm min} = 0.15\,m$. Results are presented at $mt = 105$ (Left) and 265 (Right). For $m_{\rm H} = 3m_{\rm W}$ and $ma = 0.52$.

6.2 The Higgs to W boson mass ratio

Most of the results presented in the previous sections correspond to a Higgs to W-mass ratio of 3. Qualitatively the picture remains the same for the other two ratios analyzed: $m_{\rm H} = 2\,m_{\rm W}$ and $m_{\rm H} = 4.65\,m_{\rm W}$. In Fig. 20 we compare the electromagnetic energy densities and helical susceptibility as a function of time for different values of the ratio $m_{\rm H}/m_{\rm W}$. We have chosen here not to normalize the energy densities to the total one, in order to exhibit the independence of the initial magnitude of the electromagnetic fields and helical susceptibility on the value of Higgs self-coupling λ, which also determines the mass ratio. Other features of the initial configuration such as string lengths and widths are also λ-independent, and depend only on the mass parameter M that fixes the Higgs Gaussian random field (see Appendix D). This λ-independence is preserved in the first Higgs oscillation but lost afterwards, once non-linearities and the presence of the gauge fields modifies the dynamics. At late times equipartition would indicate that the total fraction of energy density carried by the electromagnetic field would again become λ-independent. Since $\rho_0 = m^4/4\lambda$, the fraction of energy densities in units of m^4 should tend to behave as $1/\lambda$ at late times. This is indeed the tendency observed in the data.

7. Conclusions

In this paper we have analyzed the production of primordial magnetic fields in a model of low-scale EW hybrid inflation. Some partial aspects of our study were anticipated in Ref. [78]. For that purpose we have studied, with the help of lattice non-perturbative techniques, the preheating and early reheating periods after the end of a inflationary period. Our work includes, for the first time, the full Standard

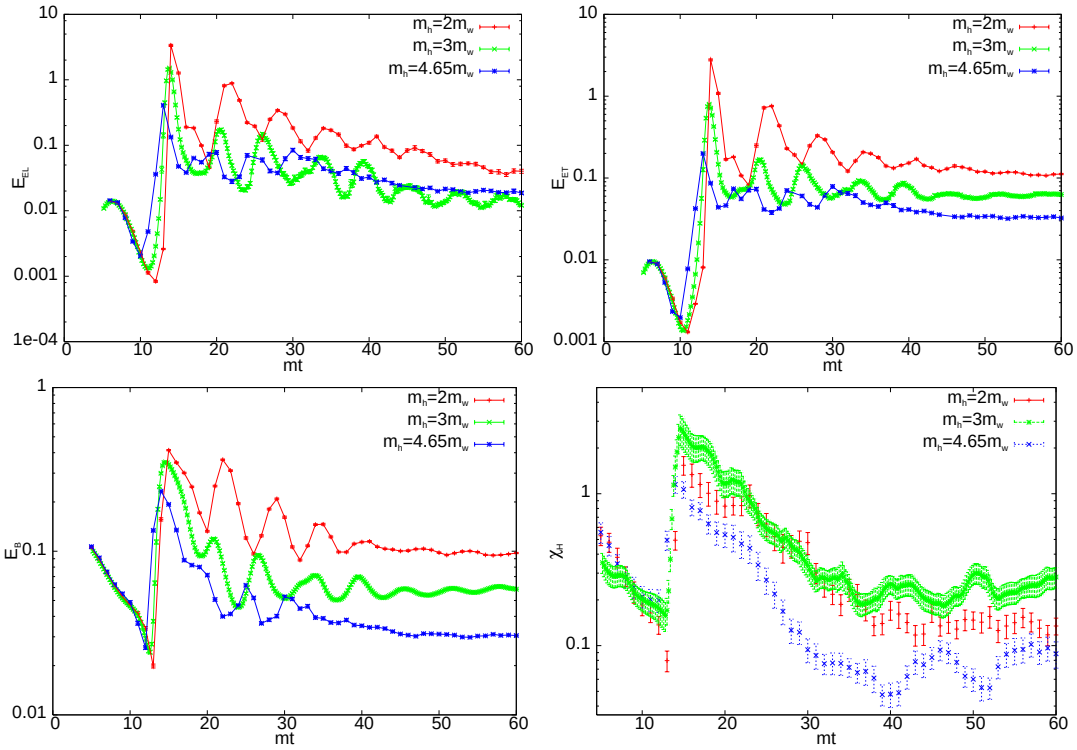

Figure 20: Time evolution of the energy densities, in m^4 units, in the: Top Left: longitudinal electric field; Top Right: transverse electric field; Bottom Left: magnetic field. Bottom Right: χ_H in m^3 units. Energy densities are not normalized to the total energy density in order to emphasize λ independence in the initial stages of the evolution.

Model, SU(2) $\otimes$ U(1), gauge degrees of freedom. The period of low-scale inflation which sets the initial conditions of our work could be brief. We do not need the full 60 e-folds that are necessary to account for the CMB anisotropies. All that is needed is a period of thermal inflation at the EW scale which would cool down the universe during at least 10 e-folds, and set the stage for a cold (quantum) EW transition. The metric fluctuations responsible for large scale structure could be produced at the primordial (high energy scale) inflation. This secondary stage only redshifts scales by another e^{10} factor, but is irrelevant for horizon size fluctuations today, while is enough to erase all relativistic and non-relativistic species. This scenario was first proposed in Ref. [70] and has recently been considered in Ref. [69].

The main results of our work can be summarized in the following three observations. First, this set up provides a concrete realization of the mechanism proposed by Vachaspati [34] and Cornwall [38], by which inhomogeneities of the Higgs field phases act as sources for the generation of magnetic fields and – this is essential – with non-trivial helicity. To the best of our knowledge this is the first time that this mechanism has been observed in a fully non-perturbative set-up. Second, the

generated magnetic field would have, when red-shifted until today, an amplitude of $\sim 0.5\,\mu$G. This is enough to explain the values of magnetic fields observed in clusters, while those in galaxies would require a small amount of enhancement via the usual dynamo mechanism. Third, the correlation length of the generated magnetic field grows linearly with time within the time span we have analyzed. For $m_{\rm H} = 3m_{\rm W}$ we find $m\xi_B \sim 0.03\,mt$, as shown in Fig. 14. This linear growth seems to be sustained by the non-trivial dynamics of the plasma made of W-bosons and could be expected to hold until the decay of the Higgs, the W and the Z bosons into light fermions. Our approach does not allow us to extrapolate these results from then onwards. Nevertheless, the helical nature of the generated magnetic field warrants that the effect of the primordial plasma would be that of preserving and even amplifying the magnitude of the helicity and the magnetic field correlation length [31]- [33].

We have distinguished three different stages in the evolution after inflation ends: tachyonic growth of the Higgs-field low momentum modes, symmetry breaking and late time evolution after SSB. In what follows we will summarize the main features characterizing each of these stages.

During the first tachyonic stage, non-linearities in the Higgs potential and gauge fields can be neglected and the quantum evolution of the system can be exactly solved. Quantum fluctuations of the Higgs-field infrared modes are described by a multi-component Gaussian random field. As described in detail in section 4, magnetic fields are already present at this stage with a non-trivial helical susceptibility directly related to the winding number susceptibility of the Higgs as a Gaussian random field. Although SU(2)$\otimes$ U(1) gauge fields are very small at the end of inflation, the magnetic fields arise through the presence of inhomogeneities in the Higgs field phase, thus corroborating Vachaspati's conjecture. Along this period, the spatial distribution of the magnetic field is determined by that of the Higgs field, a feature that is maintained and even enhanced during the second stage of evolution corresponding to symmetry breaking.

The period of SSB arises via the formation of bubbles in the Higgs field norm that expand with time and collide with each other. Magnetic fields are squeezed by the expansion in string-like structures localized in the regions between bubbles (see Fig. 4). This stringy structure is reproduced both in the helicity density and in the Z boson magnetic field density. We have estimated a characteristic string separation during this period of $m_{\rm H} l \sim 14$. Linked to the appearance of the magnetic strings we find a non trivial distribution of electric fields and W-boson charge and current densities. Most remarkably, we see a very non-trivial distribution of the charge density with the formation of extended charged clusters which track the position of the magnetic string. This separation of unequal charges induces electric fields in the plasma. We observe both transverse and longitudinal electric fields also correlated with the string locations. The clusters persist for a very long time and, as a consequence, we observe a very slow screening of the longitudinal electric field

with time, see Fig. 10. We conjecture that these electric fields will be erased as soon as the plasma of W-bosons decays into light fermions moving close to the speed of light, which will neutralize much faster than the heavy W-charges.

The third stage of evolution after SSB is characterized by a very slow approach to thermalisation. To claim a feasible mechanism for magnetogenesis we have to guarantee that the initial helical magnetic seed is not removed with time. We have shown in section 5 that the magnitude of the helical susceptibility grows with time with a power-law behaviour, $\chi_H \propto t^\alpha$, with $\alpha = 0.7(1)$, $0.8(1)$ and $0.3(1)$ for $m_{\rm H}/m_{\rm W} = 2$, 3, 4.65 respectively. At the same time the Z-boson helical susceptibility decays also with a power law dependence with time. We have observed that the magnitude of the generated magnetic susceptibility does not depend monotonically on the Higgs- to W-mass ratio. Of the values we have analyzed, $m_{\rm H}/m_{\rm W} = 3$ is the one that generates larger helical fields.

In order to extract the late time behaviour of the amplitude and correlation length of the magnetic field seed, we have performed a detailed analysis of the magnetic field Fourier spectrum for $m_{\rm H}/m_{\rm W} = 3$. It shows two well differentiated and uncorrelated components: an ultraviolet radiation sector and an infrared peak whose amplitude increases with time (see Fig. 12). The radiation tail is well described by a Bose-Einstein distribution of massive photons with a non-trivial chemical potential at temperatures $T \sim 0.23\, m_{\rm H}$ slowly rising with time. The low momentum part of the spectrum carries a fraction $f \sim 10^{-2}$ of the total energy density. As mentioned before, both its amplitude as its correlation length are linearly growing with time within the analyzed time span, showing indications of an inverse cascade towards the infrared. However, our time scales are not long enough to demonstrate that inverse cascade will be sustained at even later times when the composition of the plasma changes significantly. For the moment we can, nevertheless, rely on the results in Refs. [31]- [33] which show that helical fields are optimally amplified by MHD evolution.

In summary, hybrid preheating at the EW scale could be responsible for the observed magnetic fields associated with large scale structures like galaxies and clusters of galaxies. Both the magnitude and correlation length could be derived from the highly non-linear and non-perturbative evolution after EW symmetry breaking. Our analysis provides a concrete realization of the mechanism proposed by Vachaspati and Cornwall many years ago. This primordial plasma enters a regime in which helical magnetic field lines experience an inverse cascade towards larger scales. We observe how both their energy density and correlation length grow linearly with time. Showing that these magnetic fields evolve as described in the introduction until photon decoupling would require a detailed follow up with MHD simulations with initial conditions provided by our work. This result would support our proposal that the helical magnetic fields produced at the cold EW transition are responsible for the observed magnetic fields in galaxies and clusters of galaxies.

Acknowledgements

It is a pleasure to thank G. Aarts, A. Achúcarro, J. Berges, J.M. Cornwall, M. Hindmarsh, A. Kusenko, M. Salle, J. Smit, J. Urrestilla and T. Vachaspati for lively discussions. JGB thanks the Kavli Institute for Theoretical Physics, for hospitality during the last stages of the work, and the organisers of the "Nonequilibrium Dynamics in Particle Physics and Cosmology 2008" programme for the invitation. We acknowledge financial support from the Madrid Regional Government (CAM) under the program HEPHACOS P-ESP-00346, and the Spanish Research Ministry (MEC) under contracts FPA2006-05807, FPA2006-05485, FPA2006-05423, FPA2006-26414-E. This work was supported in part by the (US) National Science Foundation under Grant No. PHY05-51164. We also acknowledge use of the MareNostrum supercomputer at the BSC-CNS and the IFT-UAM/CSIC computation cluster. The authors participate in the Consolider-Ingenio 2010 CPAN (CSD2007-00042) and PAU (CSD2007-00060).

A. The Lattice Equations of Motion

To solve the classical equations of motion we discretise them on a lattice preserving full gauge invariance. In this appendix we introduce the lattice notation and derive the lattice equations of motion for our particular problem.

As usual, the lattice points are labeled by a vector of integers $n = (n_0, \vec{n})$ in terms of which the space-time positions are given by: $x = (n_0\, a_t, \vec{n}\, a)$, with a_t and a the temporal and spatial lattice spacings related by $\kappa = a_t/a$. The adimensional lattice scalar fields are derived from the continuum ones as: $\Phi_L(n) = a\,\Phi(x/a)$ and $\chi_L(n) = a\,\chi(x/a)$. In what follows we will omit the subscript L, since all fields will be lattice fields unless explicitly indicated. The Higgs field is expanded as: $\Phi(n) = \sum_\alpha \phi^\alpha(n)\,\bar{\sigma}_\alpha$, in the basis of 2×2 SU(2) matrices: $\bar{\sigma} \equiv (\mathbb{1}, i\vec{\tau})$, with τ_a the Pauli matrices and ϕ^α real coefficients. The Standard Model Higgs doublet is obtained trough the projection: $\varphi = \Phi\,(1,0)^T$. Gauge fields are given in terms of link variables: $U_\mu(n)$ and $B_\mu(n)$ for SU(2) and hypercharge fields respectively. They are both 2×2 SU(2) matrices, with the peculiarity that $B_\mu(n)$ is diagonal. Expanded in the $\bar{\sigma}$ basis, they read:

$$U_\mu(n) = \sum_{\alpha=0,\cdots,3} u^\alpha_\mu(n)\,\bar{\sigma}_\alpha\ ,\ B_\mu(n) = \sum_{\alpha=0,3} b^\alpha_\mu(n)\,\bar{\sigma}_\alpha\ , \tag{A.1}$$

with u^α_μ and b^α_μ real coefficients. The continuum limit of the gauge links is as usual:

$$\begin{aligned} U_\mu(n) &\sim e^{\frac{i}{2}\,a_\mu g_{\rm W} \mathcal{A}^a_\mu \tau_a}\,, \\ B_\mu(n) &\sim e^{\frac{i}{2}\,a_\mu g_{\rm Y} \mathcal{B}_\mu \tau_3}\,, \end{aligned} \tag{A.2}$$

where there is no implicit sum in the μ index and where the vector $a_\nu \equiv \{a_t, a, a, a\}$.

With the previous conventions, the usual U(1) hypercharge transformation is implemented by acting on the Φ field with right multiplication by a diagonal SU(2) matrix:

$$\varphi'(n) = e^{i\alpha(n)}\,\varphi(n) \;\longrightarrow\; \Phi'(n) = \Phi(n)\,e^{i\alpha(n)\tau_3}\,. \tag{A.3}$$

The complete SU(2)$\otimes$ U(1) gauge transformation for the Higgs field then reads:

$$\Phi(n) \to \Omega(n)\Phi(n)\Lambda(n)\,, \tag{A.4}$$

where $\Lambda(n) = \exp(i\alpha(n)\tau_3)$ represents the U(1) gauge transformation and $\Omega(n) = \sum_\alpha \Omega^\alpha(n)\,\bar{\sigma}_\alpha$ the SU(2) one. The corresponding transformations of the gauge links are:

$$\begin{aligned} U_\mu(n) &\to \Omega(n)\,U_\mu(n)\,\Omega^\dagger(n+\mu)\,, \\ B_\mu(n) &\to \Lambda(n)\,B_\mu(n)\,\Lambda^\dagger(n+\mu)\,, \end{aligned} \tag{A.5}$$

where $\hat{\mu}$ is the unit vector in the μ direction.

It is useful to introduce a lattice covariant derivative operator defined by:

$$(D_\mu\Phi)(n) = U_\mu(n)\,\Phi(n+\hat{\mu})\,B_\mu(n) - \Phi(n)\,, \tag{A.6}$$

and its adjoint:

$$(\bar{D}_\mu\Phi)(n) = U_\mu^\dagger(n-\hat{\mu})\,\Phi(n-\hat{\mu})\,B_\mu^\dagger(n-\hat{\mu}) - \Phi(n)\,. \tag{A.7}$$

In addition we introduce forward and backward ordinary lattice derivatives given by:

$$(\Delta_\mu f)(n) = f(n+\hat{\mu}) - f(n)\,, \tag{A.8}$$

$$(\bar{\Delta}_\mu f)(n) = f(n-\hat{\mu}) - f(n)\,. \tag{A.9}$$

The discretization of the pure gauge part of the Lagrangian is done in terms of the plaquette fields:

$$\begin{aligned} P_{\mu\nu}(n) &= U_\mu(n)\,U_\nu(n+\hat{\mu})\,U^\dagger(n+\hat{\nu})\,U^\dagger(n)\,, \\ P_{\mu\nu}^{ab}(n) &= B_\mu(n)\,B_\nu(n+\hat{\mu})\,B^\dagger(n+\hat{\nu})\,B^\dagger(n)\,, \end{aligned} \tag{A.10}$$

with the transformation properties:

$$\begin{aligned} P_{\mu\nu}(n) &\to \Omega(n)\,P_{\mu\nu}(n)\,\Omega^\dagger(n)\,, \\ P_{\mu\nu}^{ab}(n) &\to \Lambda(n)\,P_{\mu\nu}^{ab}(n)\,\Lambda^\dagger(n) = P_{\mu\nu}^{ab}(n)\,. \end{aligned} \tag{A.11}$$

The pure gauge discretized Lagrangian then reads:

$$L_{\rm Y}(n) = \frac{2}{\kappa g_Y^2}\sum_i \mathrm{Tr}\,[1 - P_{0i}^{ab}(n)] - \frac{\kappa}{g_Y^2}\sum_{i\neq j}\mathrm{Tr}\,[1 - P_{ij}^{ab}(n)]\,, \tag{A.12}$$

$$L_{\rm SU(2)}(n) = \frac{2}{\kappa g_W^2}\sum_i \mathrm{Tr}\,[1 - P_{0i}(n)] - \frac{\kappa}{g_W^2}\sum_{i\neq j}\mathrm{Tr}\,[1 - P_{ij}(n)]\,. \tag{A.13}$$

And the complete lattice Lagrangian is:

$$L_{\rm L}(n) = L_{\rm Y}(n) + L_{\rm SU(2)}(n) + {\rm Tr}\Big\{ ({\rm D}_\mu\Phi)^\dagger({\rm n})\,({\rm D}^\mu\Phi)({\rm n}) \Big\} + \frac{1}{2}\Delta_\mu\chi(n)\,\Delta^\mu\chi(n) - \kappa\, V(\Phi(n),\chi(n))\,, \tag{A.14}$$

where all the derivatives are lattice derivatives and all matter fields are adimensional lattice fields. To simplify notation we have introduced the lattice metric tensor $\eta^{\mu\nu}$ with non-zero elements: $\eta^{00} = 1/\kappa$ and $\eta^{ii} = -\kappa$, $i = 1, 2, 3$. This allows to raise four-dimensional indices in the usual way. The potential, $V(\Phi(n), \chi(n))$, has the explicit form:

$$V(\Phi(n),\chi(n)) = -\, M_L^2\,{\rm Tr}\{\Phi^\dagger({\rm n})\Phi({\rm n})\} + \lambda\left({\rm Tr}\{\Phi^\dagger({\rm n})\Phi({\rm n})\}\right)^2 + \frac{\mu_L^2}{2}\,\chi^2(n) + g^2\chi^2(n)\,{\rm Tr}\{\Phi^\dagger({\rm n})\Phi({\rm n})\}\,, \tag{A.15}$$

with $M_L = a\,m$, $\mu_L = a\,\mu$, and where g and λ are the same coupling constants appearing in the continuum Lagrangian.

We have now all the necessary ingredients to write the lattice equations of motion. They are derived by imposing that the variation of the lattice action with respect to each of the fields in the Lagrangian vanishes. We obtain:

$$\begin{aligned}
(\Delta_\mu\bar{\Delta}^\mu\chi)(n) &= \kappa\left\{\mu_L^2 + 2g^2\,{\rm Tr}[\Phi^\dagger({\rm n})\Phi({\rm n})]\right\}\chi({\rm n})\,, \\
(D_\mu\bar{D}^\mu\Phi)(n) &= \kappa\left\{ -\,M_L^2 + g^2\,\chi^2(n) + 2\lambda\,{\rm Tr}[\Phi^\dagger({\rm n})\Phi({\rm n})]\right\}\Phi({\rm n}), \\
(\bar{D}^{\rm A}_\nu\,G^{\mu\nu})(n) &= \kappa\,J^\mu(n)\,, \\
(\bar{D}^{Y}_\nu\,F^{\mu\nu})(n) &= \kappa\,J^\mu_{\rm Y}(n)\,,
\end{aligned} \tag{A.16}$$

with the currents given by:

$$\begin{aligned}
J^\mu(n) &= \frac{ig_W}{2}\left[\Phi(n)\,(D^\mu\Phi)^\dagger(n) - (D^\mu\Phi)(n)\,\Phi^\dagger(n)\right], \\
J^\mu_Y(n) &= \frac{ig_Y}{2}\left[(D^\mu\Phi)^\dagger(n)\,\Phi(n) - \Phi^\dagger(n)\,(D^\mu\Phi)(n)\right]_3\bar{\sigma}_3/2\,,
\end{aligned} \tag{A.17}$$

where the sub-index 3 in the second equation denotes the component, of the term between brackets, along $\bar{\sigma}_3/2$. The covariant derivatives, $(D_\mu\Phi)(n)$ and $(\bar{D}_\mu\Phi)(n)$, are given by Eqs. (A.6), (A.7). We have also introduced two additional covariant derivative operators: D^A_μ and D^Y_μ, obtained from the standard one by setting either the hypercharge or the SU(2) gauge links to the identity, i.e.:

$$\begin{aligned}
(D^{\rm A}_\mu\Phi)(n) &= U_\mu(n)\,\Phi(n+\hat{\mu}) - \Phi(n)\,, \\
(D^{\rm Y}_\mu\Phi)(n) &= \Phi(n+\hat{\mu})\,B_\mu(n) - \Phi(n)\,.
\end{aligned} \tag{A.18}$$

The corresponding expressions for the plaquette fields are:

$$
\begin{aligned}
(D^{\mathrm{A}}_{\mu} P_{\rho\nu})(n) &= U_{\mu}(n)\, P_{\rho\nu}(n+\hat{\mu})\, U^{\dagger}_{\mu}(n) - P_{\rho\nu}(n)\,, \\
(D^{\mathrm{Y}}_{\mu} P^{ab}_{\rho\nu})(n) &= P^{ab}_{\rho\nu}(n+\hat{\mu}) - P^{ab}_{\rho\nu}(n)\,.
\end{aligned}
\tag{A.19}
$$

The tensors $G_{\mu\nu}$ and $F_{\mu\nu}$, appearing in the equations of motion, are defined from the traceless part of the plaquettes by:

$$
\begin{aligned}
F_{\mu\nu} &= \frac{i}{2g_Y}[P^{ab}_{\mu\nu}(n) - P^{ab}_{\nu\mu}(n)]\,, \\
G_{\mu\nu} &= \frac{i}{2g_W}[P_{\mu\nu}(n) - P_{\nu\mu}(n)]\,.
\end{aligned}
\tag{A.20}
$$

In order to simplify the problem of solving the lattice equations of motion it is convenient to fix the temporal gauge, realized on the lattice by fixing the temporal component of the hypercharge and SU(2) links to unity: $B_0(n) = \mathbb{1}$, $U_0(n) = \mathbb{1}$. In this gauge, the lattice equations of motion can be used to solve for the fields at time $n_0 + 2$ in terms of the fields at times n_0 and $n_0 + 1$. The lattice equations associated to the gauge fixed degrees of freedom become constraint equations analogous to the continuum Gauss law:

$$
\begin{aligned}
(\bar{D}^{\mathrm{A}}_{k} G^{0k})(n) &= \kappa\, J^{0}(n)\,, \\
(\bar{D}^{\mathrm{Y}}_{k} F^{0k})(n) &= \kappa\, J^{0}_{Y}(n)\,.
\end{aligned}
\tag{A.21}
$$

As proved in Ref. [74], these constraints are preserved by the lattice evolution. It is hence sufficient to impose them on the initial conditions. The way this is done for our numerical simulations follows exactly the procedure described in Ref. [74] for SU(2) where we refer the reader for further details.

B. Lattice version of the Maxwell equations

In this appendix we present the derivation of the lattice version of the Maxwell equations used in order to define the W charge and current densities. Starting from the continuum expressions:

$$
\begin{aligned}
&\vec{\nabla}\vec{E}(x) = \rho(x) \quad , \quad \vec{\nabla}\vec{j}(x) + \partial_0\, \rho(x) = 0 \\
&\vec{\nabla}\vec{B}(x) = 0 \\
&\vec{\nabla} \times \vec{E}(x) + \partial_0\, \vec{B}(x) = 0 \\
&\vec{\nabla} \times \vec{B}(x) - \partial_0\, \vec{E}(x) = \vec{j}(x)\,.
\end{aligned}
\tag{B.1}
$$

we look for a discretization that preserves the Bianchi identities.

In section 3.2, we have defined the electromagnetic lattice field strength, $F^{\gamma}_{\mu\nu}(n)$, in terms of clover averaged Z and B field strengths. The clover average of a space-time tensor, like $F_{0i}(n)$, is given by:

$$\langle F_{0i}(n)\rangle_{\rm clov} \equiv \frac{1}{2}\Big(F_{0i}(n) + F_{0i}(n-\hat{0})\Big)\,, \tag{B.2}$$

while for a spatial tensor we have:

$$\langle F_{ij}(n)\rangle_{\rm clov} \equiv \frac{1}{4}\Big(F_{ij}(n) + F_{ij}(n-\hat{\imath}) + F_{ij}(n-\hat{\jmath}) + F_{ij}(n-\hat{\imath}-\hat{\jmath})\Big)\,. \tag{B.3}$$

From them we extract the lattice electric and magnetic fields:

$$E_i(n) = \frac{1}{e\,a a_t}\,\langle F_{i0}(n)\rangle_{\rm clov}\;, \quad B_i(n) = \frac{1}{2\,e\,a^2}\,\epsilon_{ijk}\,\langle F_{jk}(n)\rangle_{\rm clov}\,. \tag{B.4}$$

The electromagnetic $\vec{E}$ and $\vec{B}$ fields, defined above, verify the following Bianchi identities:

$$\vec{\Delta}^I\cdot\vec{B}(n) = 0\;, \quad \vec{\Delta}^I\times\vec{E}(n) + \frac{1}{\kappa}\,\Delta_0\vec{B}(n) = 0\,, \tag{B.5}$$

where we have introduced an improved lattice derivative given by:

$$(\Delta^I_\mu f)(n) = \frac{1}{2}\Big(f(n+\hat{\mu}) - f(n-\hat{\mu})\Big)\,. \tag{B.6}$$

We now define accordingly the longitudinal and transverse components of the electromagnetic fields. The projection is done in momentum space with Fourier transformed fields:

$$\vec{E}(\vec{k}) = \int d^3\vec{x}\;\vec{E}(\vec{x})\,e^{-i\vec{k}\cdot\vec{x}}\;,\;\; \vec{B}(\vec{k}) = \int d^3\vec{x}\;\vec{B}(\vec{x})\,e^{-i\vec{k}\cdot\vec{x}}\,, \tag{B.7}$$

with lattice momenta: $k_i = 2\pi n_i/(N_s\,a)$, $n_i\in\mathbb{Z}$. Transverse components, $\vec{A}_t$, of a vector $\vec{A}$, are defined such that $\hat{q}\cdot\vec{A}_t = 0$, where:

$$\vec{q} = \frac{1}{2}\,(\vec{v}-\vec{v}^*), \quad \text{with}\;\; v_i = \frac{1}{a}\,(e^{-ik_i a}-1)\,, \tag{B.8}$$

and with $\hat{q}$ the unit vector in the direction of $\vec{q}$.

The electromagnetic, Fourier transformed, charge and current densities are computed through:

$$\rho\,(\vec{k}) = \hat{q}\cdot\vec{E}(\vec{k})\,, \tag{B.9}$$

$$\vec{\jmath}(\vec{k}) = \hat{q}\times\vec{B}(\vec{k}) - \frac{1}{a_t}\,\bar{\Delta}_0\;\vec{E}(\vec{k})\,. \tag{B.10}$$

C. Thermal radiation

In the present appendix, we prove the relation:

$$\langle|\vec{B}(\vec{x})|^{2n}\rangle = \langle: |\vec{B}(\vec{x})|^{2n} :\rangle_{Q(T)} \ , \tag{C.1}$$

where the left side of the equality is calculated using the Maxwellian classical distribution:

$$\langle|\vec{B}|^{2n}\rangle = \sqrt{\frac{2}{\pi}}\Big(\frac{3}{\langle B^2\rangle}\Big)^{3/2}\int_0^\infty dB B^{2n+2} e^{-\frac{B^2}{\frac{2}{3}\langle B^2\rangle}} \ , \tag{C.2}$$

whereas the right hand side is calculated using the thermal quantum distribution in the canonical formalism. Thus,

$$\langle: |\vec{B}(\vec{x})|^{2n} :\rangle_{Q(T)} \equiv \frac{\mathrm{Tr}(: |\vec{B}(\vec{x})|^{2n} : \rho)}{\mathrm{Tr}(\rho)}. \tag{C.3}$$

where ρ is the canonical distribution density matrix:

$$\rho = e^{-\frac{H}{T}}. \tag{C.4}$$

and $: O :$ denotes normal ordering of the operator O. By performing the integral in Eq. C.2 we obtain the classical thermal averages:

$$\langle|\vec{B}(\vec{x})|^{2n}\rangle = \frac{(2n+1)!!}{3^n}(\langle|\vec{B}(\vec{x})|^2\rangle)^n. \tag{C.5}$$

Our goal is then to compute the thermal quantum averages

$$\langle: (\vec{B}(\vec{x})\cdot\vec{B}(\vec{x}))^n :\rangle_{Q(T)}$$

on the canonical distribution at temperature T. The only terms of the normal-ordered operator that contribute to the expectation values must be diagonal in momentum space. If we single out that part we obtain

$$: (\vec{B}(\vec{x})\cdot\vec{B}(\vec{x}))^n := \prod_{i=1}^n \left(\sum_{a_i}\int d\vec{k_i}\mathbf{a}^\dagger_{a_i}(\vec{k_i})\mathbf{a}_{a_i}(\vec{k_i})\right) G_{a_1\ldots a_n}(\vec{k_1},\ldots\vec{k_n}) + X \ , \tag{C.6}$$

where X denotes the part that does not contribute to the expectation value and G is a a coefficient to be specified later.

Next we can evaluate the thermal average of the operator part, which can be expressed as a product of $\overline{n}(k_i,a_i)$, the mean number of photons of momenta $\vec{k_i}$ and polarization a_i. Hence, we arrive at

$$\prod_{i=1}^n \left(\sum_{a_i}\int d\vec{k_i}\,\overline{n}(k_i,a_i)\right) G_{a_1\ldots a_n}(\vec{k_1},\ldots\vec{k_n}) \ .$$

Now we should unfold the form of the coefficient G. It is given by

$$\frac{1}{n!}\prod_i \left(v_{l_{2i-1}}(\vec{k_i},a_i)v_{l_{2i}}(\vec{k_i},a_i)\right)\sum_{\sigma\in S_{2n}}\delta_{l_{\sigma(1)}l_{\sigma(2)}}\cdots\delta_{l_{\sigma(2n-1)}l_{\sigma(2n)}}\ ,$$

where the sum is over all the permutations of the 2n indices, and

$$v_i(\vec{k},a)=\frac{1}{(2\pi)^{3/2}\sqrt{2k}}(\vec{k}\times\vec{\epsilon}_a(\vec{k}))_i\ .$$

The sum over all permutations follows from taking all creation annihilation operators as distinguishable and assigning them to each of the $2n$ magnetic fields. Nonetheless, since we are integrating over all values of momenta one has to divide by $n!$ to eliminate double-counting.

Now we will introduce the matrix M, given by

$$M_{ij}\equiv\sum_a\int d\vec{k}\,\overline{n}(k,a)v_i(\vec{k},a)v_j(\vec{k},a)=\lambda\delta_{ij}\ . \tag{C.7}$$

The left-hand side is a consequence of rotational invariance. Substituting in the previous formulas we get

$$\frac{1}{n!}M_{l_1l_2}\cdots M_{l_{2n-1}l_{2n}}\sum_{\sigma\in S_{2n}}\delta_{l_{\sigma(1)}l_{\sigma(2)}}\cdots\delta_{l_{\sigma(2n-1)}l_{\sigma(2n)}}\ .$$

The sum over permutations can be factored as follows

$$\sum_{\sigma\in S_{2n}}\delta_{l_{\sigma(1)}l_{\sigma(2)}}\cdots\delta_{l_{\sigma(2n-1)}l_{\sigma(2n)}}=2^n n!\sum_{\text{pairings}}\prod_{\text{pair}}\delta(\text{pair})\ ,$$

where a pairing is an arrangement of the $2n$ indices into pairs (equivalently a permutation made entirely of 2-cycles). The rest of the calculation is very much like a calculation to nth order in perturbation theory in a model with 2-leg vertices given by the M matrix and a propagator given by the identity matrix. All diagrams are now characterized by n_l, the number of l-cycles (loops), where l runs from 1 to n. Applying the standard Feynman rules one arrives at

$$4^n n!\prod_i\left(\sum_{n_l}\frac{\mathrm{Tr}M^{n_l}}{(2l)^{n_l}n_l!}\right)\ .$$

The factors $2l$ and $n_l!$ provide the order of the symmetry group of the diagram. The $2l$ term is associated with cyclic permutations of the vertices and to a change in orientation. In the previous formula, the sum over n_l runs over all possible integers subject to the constraint $\sum_l ln_l=n$. One can actually perform this sum. Setting $M=\lambda\mathbf{I}$ our expression becomes proportional to λ^n. Thus, we can eliminate the

constraint on the n_l by summing over n. The constrained sum can be obtained from the unconstrained one by selecting the term proportional to λ^n. Hence,

$$4^n n! \prod_l \left(\sum_{n_l} \left(\frac{D\lambda^l}{2l} \right)^{n_l} \frac{1}{n_l!} \right) = 4^n n! \exp\{D/2 \sum_l \frac{\lambda^l}{l}\} = 4^n n! (1-\lambda)^{-D/2}$$

where D is the space dimension, which is 3 in our case. This quantity is the generating function of all the quantum averages. Differentiating n times with respect to λ we extract the n-th term that we were looking for:

$$\langle : (\vec{B}(\vec{x}) \cdot \vec{B}(\vec{x}))^n : \rangle_{Q(T)} = (2\lambda)^n (2n+1)!! \tag{C.8}$$

The result for $D = \lambda = 1$, given by $\frac{(2n)!}{n!}$, serves to crosscheck the result. From the previous equation (C.8) we get $\lambda = (1/6)\langle : |B|^2(v) : \rangle_{Q(T)}$ allowing to re-express eq. (C.8) in the form of eq. (C.5).

To conclude we give the expression of $\langle : |B(\vec{x})|^2 : \rangle_{Q(T)}$ in terms of the temperature. Taking the trace of eq. (C.7) we obtain:

$$\langle : |B|^2(x) : \rangle_{Q(T)} = \int d\vec{k} \frac{1}{(2\pi)^3} 2\, k\, \overline{n}(k,a)\,.$$

Taking into account $\overline{n}(k,a) = (e^{k/T} - 1)^{-1}$, we can perform the integration:

$$\frac{1}{\pi^2} \int dk k^3 \frac{1}{(e^{k/T}-1)} = \frac{1}{\pi^2} \int dk k^3 \sum_{n=1}^{\infty} -(e^{-k/T})^n = \frac{6}{\pi^2} T^4 \sum_{n=1}^{\infty} \frac{1}{n^4}.$$

The sum over n is the known $\zeta(4) = \pi^4/90$, leading to:

$$\frac{1}{2} \langle : |B|^2(x) : \rangle_{Q(T)} = \frac{\pi^2}{30} T^4$$

D. Gaussian Random fields

In this appendix we revisit the predictions of the Gaussian random field model. As explained in Section 3 of the paper, the initial conditions produced by the quantum evolution shortly after inflation ends are of this type. Furthermore, this distribution seeds the generation of magnetic fields and Chern-Simons number. There is an extensive literature (see Refs. [86]-[89]) on Gaussian random fields and some of the analytic predictions have been included in our previous papers. However, here we are dealing with multicomponent fields and some of the predictions and methodology do not hold in this case. Besides, there are many more relevant observables directly related to the Physics issues addressed in this paper. To explore these matters within this paper, we have felt satisfied with its numerical study. Since gauge fields and non-linearities do not play a role at this stage, we have profited to increase statistics

and test systematic errors at a low computational cost. These results can then be used as a reference to compare with our full-theoretical ones.

Our Gaussian random field is homogeneous and isotropic. The power spectrum was set to match the one produced by the quantum evolution of the Higgs field coupled to a linearly time-dependent inflaton and neglecting the Higgs self-interaction. The details and nomenclature are explained in our previous paper [73]. We recall that the Higgs field has 4 real components which are independent random variables with identical power spectrum which, for simplicity, is fitted to a simple form which reproduces nicely its shape:

$$P(k,t) = \frac{1}{2m^2\pi^2} k^2 (A(t) e^{-B(t)\,k^2/m^2} + 1)\Theta(\sqrt{2Vtm} - k) \tag{D.1}$$

where V is the inflaton velocity at the end of inflation, A and B are time-dependent parameters and Θ is the Heaviside step function.

It is interesting to be able to trace the dependence of our results on the different parameters that enter our model. Fortunately, this dependence is greatly encoded in two scales that characterize the Gaussian random field. One scale fixes the magnitude of the Higgs field. We choose this scale to be the dispersion σ of the field at one spatial point. Notice that the physical scale v, giving the expectation value of the Higgs field in the true vacuum, has not yet entered the scene, since the Gaussian random field is generated before the self-interaction of the Higgs field affects the evolution. It is precisely the comparison between $\sigma(t)$ and v that must be taken into account in fixing the range of values of the initial times t_i for the subsequent non-linear classical evolution of the system.

In addition, the other scale of the problem is a length scale ξ_0 associated to the Gaussian random field as follows:

$$\frac{1}{\xi_0^2} \equiv \frac{\int \frac{dk}{k} P(k,t) k^2}{\int \frac{dk}{k} P(k,t)} \tag{D.2}$$

With our choice of velocity $V = 0.024$ at $mt_i = 5$ we obtain $\sigma = 0.139\, v$, for $m_{\rm H} = 3m_{\rm W}$. Thus, we are safely in the region where non-linearities are still small. On the other hand $m\xi_0 = 3.09$, which determines the adequate ranges of the ultraviolet and infrared cut-off of our numerical procedure. At $mt_i = 6.5$ these numbers have changed to $\sigma = 0.204\, v$ and $m\xi_0 = 2.95$ respectively. This observation allows us to give results in a way that are valid for all the values of initial times employed in this work.

In line with previous analysis, we will present our results for the density and distribution of local maxima of $|\phi|$. The density of maxima is given by $0.0140(4)\, \xi_0^{-3}$. The distribution of minimum distances among maxima can be studied directly and displays an approximate Gaussian distribution with mean $3.1(1)\, \xi_0$ and dispersion $0.62(2)\, \xi_0$. We have also studied the distribution of values of $|\phi|$ at the maxima, φ.

The average height of a peak being $1.52(4)\sigma$. The histogram is much narrower than the one obtained for a single component Gaussian random field, and is well-fitted to the following expression

$$\varphi^a \exp\left\{-\frac{\varphi^2}{2\tilde{\sigma}^2}\right\}$$

with $a = 10.4(5)$ and $\tilde{\sigma} = 0.44(1)\,\sigma$. Nicely enough the results presented are robust as one changes the ultraviolet, infrared cut-offs and time within their safe windows (See Fig. 21). Errors quoted are both statistical and systematic.

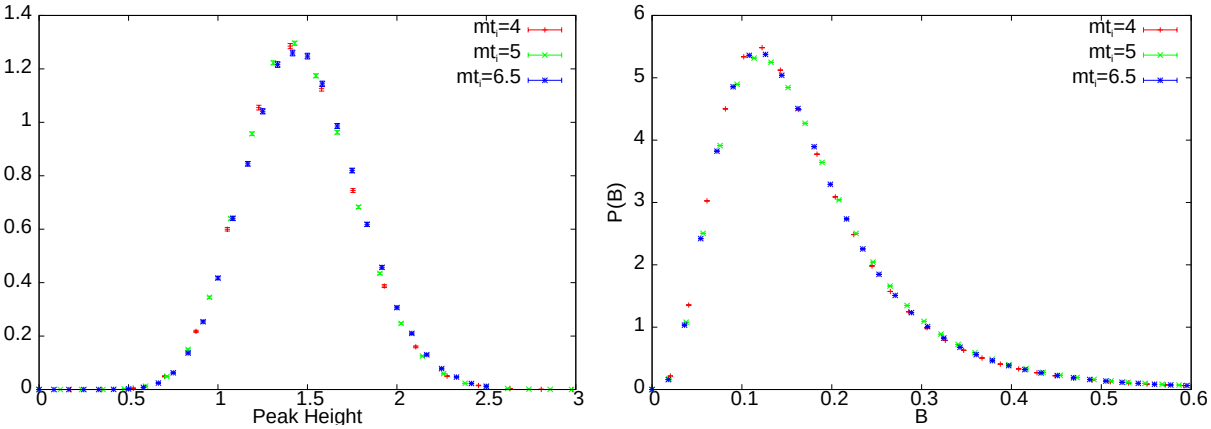

Figure 21: Left: Histogram of peak (local maxima) heights, expressed in $\sigma(t_i)$ units. Right: Distribution of the the local magnetic field intensity $B = |\vec{B}(x)|$ in $\xi_0(t_i)$ units.

Now we turn to observables which are characteristic of multi-component Gaussian random fields. A crucial role is played by the topological susceptibility χ which is obtained by dividing the mean value of the winding number square by the volume. We obtain $1.55(10) \times 10^{-3}\xi_0^{-3}$. We can also compute the initial magnetic field distribution. Notice that, as explained in the paper, despite the fact that SU(2)×U(1) gauge fields are zero at this stage, our formulas induce a non-zero Z field and a non-zero magnetic field which is proportional to it. Computing this magnetic field at each point of space we obtain a distribution which is well fitted by a formula

$$P(B) = B^b \exp\left\{-\left(\frac{B}{d_1}\right)^{h_1}\right\} + A\,\exp\left\{-\left(\frac{B}{d_2}\right)^{h_2}\right\}\,,$$

with $B = |\vec{B}(x)|$, see Fig. 13. Our best fit values of the parameters are $b = 1.89(3)$, $d_1\,\xi_0^2 = 3.0(1)\,10^{-3}, h_1 = 0.368(3)$, $d_2\,\xi_0^2 = 2.61(2), h_2 = 1.34(3)$, $A = 1.0(5)\,10^{-7}$. The initial magnetic field distribution has a slower decrease at large values than the Maxwellian distribution obtained at later times. The aforementioned universality can be tested here. In particular, it follows that results obtained at different initial

times t_i should fall in the same curve once normalised by the scales of σ and ξ_0. This is clearly seen in Fig. 21.

We have also studied the spectrum of the magnetic field to compare it with the one obtained once non-linearities set in. In our case the high momentum profile differs from the thermal tail displayed at later times. Instead, the high momentum tail is well fitted by a function

$$\exp\left\{-\left(\frac{k}{b}\right)^c\right\}$$

where $b\xi_0 = 0.01(1)$ and $c = 0.36(4)$.

References

[1] E. N. Parker, "Cosmological Magnetic Fields," Clarendon Press, Oxford (1979)

[2] Ya. B. Zeldovich, A. A. Ruzmaikin and D. D. Sokoloff, "Magnetic Fields in Astrophysics," Gordon and Breach, New York (1983)

[3] A. A. Ruzmaikin, A. M. Shukurov and D. D. Sokoloff, "Magnetic Fields of Galaxies," Kluwer Academic Publisher, Dordrecht (1988)

[4] D. Biskamp, "Non-linear magnetohydrodynamics," Cambridge U.P., Cambridge (1994)

[5] P. P. Kronberg, "Extragalactic magnetic fields," Rept. Prog. Phys. **57**, 325 (1994).

[6] R. Beck, A. Brandenburg, D. Moss, A. Shukurov and D. Sokoloff, "Galactic Magnetism: Recent developments and perspectives," Ann. Rev. Astron. Astrophys. **34**, 155 (1996).

[7] K. Enqvist, "Primordial magnetic fields," Int. J. Mod. Phys. D **7**, 331 (1998) [arXiv:astro-ph/9803196].

[8] R. M. Kulsrud, "A Critical Review Of Galactic Dynamos," Ann. Rev. Astron. Astrophys. **37**, 37 (1999).

[9] D. Grasso and H. R. Rubinstein, "Magnetic fields in the early universe," Phys. Rept. **348**, 163 (2001) [arXiv:astro-ph/0009061]

[10] C. L. Carilli and G. B. Taylor, "Cluster Magnetic Fields," Ann. Rev. Astron. Astrophys. **40**, 319 (2002) [arXiv:astro-ph/0110655]

[11] J. L. Han and R. Wielebinski, "Milestones in the Observations of Cosmic Magnetic Fields," Chin. J. Astron. Astrophys. **2**, 293 (2002) [arXiv:astro-ph/0209090]

[12] L. M. Widrow, "Origin of Galactic and Extragalactic Magnetic Fields," Rev. Mod. Phys. **74**, 775 (2003) [arXiv:astro-ph/0207240].

[13] M. Giovannini, "The magnetized universe," Int. J. Mod. Phys. D **13**, 391 (2004) [arXiv:astro-ph/0312614].

[14] B. M. Gaensler, R. Beck and L. Feretti, "The Origin and Evolution of Cosmic Magnetism," New Astron. Rev. **48**, 1003 (2004) [arXiv:astro-ph/0409100].

[15] M. Shaposhnikov, "Primordial magnetic fields," AIP Conf. Proc. **784** (2005) 423.

[16] R. Beck, "Magnetic fields in galaxies," Lecture Notes in Physics **664**, 41 (2005)

[17] R. Durrer, "Cosmic Magnetic Fields and the CMB," New Astron. Rev. **51**, 275 (2007) [arXiv:astro-ph/0609216]

[18] J. D. Barrow, R. Maartens and C. G. Tsagas, "Cosmology with inhomogeneous magnetic fields," Phys. Rept. **449**, 131 (2007) [arXiv:astro-ph/0611537]

[19] R. Durrer and C. Caprini, "Primordial Magnetic Fields and Causality," JCAP **0311**, 010 (2003) [arXiv:astro-ph/0305059]

[20] J. Vallée, "Observations of the Magnetic Fields Inside and Outside the Milky Way," Fund. Cosm. Phys. **19**, 1 (1997)

[21] A. Dar and A. De Rujula, "The Magnetic Field in Galaxies, Galaxy Clusters, and the InterGalactic Space," Phys. Rev. D **72**, 123002 (2005) [arXiv:astro-ph/0504480]

[22] J. M. Quashnock, A. Loeb and D. N. Spergel, Astrophys. J. 344 (1989) L49.

[23] C. J. Hogan, "Magnetohydrodynamic effects of a first-order cosmological phase transition," Phys. Rev. Lett. **51**, 1488 (1983).

[24] B. l. Cheng and A. V. Olinto, "Primordial magnetic fields generated in the quark - hadron transition," Phys. Rev. D **50**, 2421 (1994).

[25] G. Sigl, A. V. Olinto and K. Jedamzik, "Primordial magnetic fields from cosmological first order phase transitions," Phys. Rev. D **55**, 4582 (1997) [arXiv:astro-ph/9610201].

[26] J. Ahonen and K. Enqvist, "Magnetic field generation in first order phase transition bubble collisions," Phys. Rev. D **57**, 664 (1998) [arXiv:hep-ph/9704334]

[27] G. Baym, D. Bodeker and L. D. McLerran, "Magnetic fields produced by phase transition bubbles in the electroweak phase transition," Phys. Rev. D **53**, 662 (1996) [arXiv:hep-ph/9507429].

[28] M. Hindmarsh and A. Everett, "Magnetic fields from phase transitions," Phys. Rev. D **58**, 103505 (1998) [arXiv:astro-ph/9708004].

[29] A. Brandenburg, K. Enqvist and P. Olesen, "Large-scale magnetic fields from hydromagnetic turbulence in the very early universe," Phys. Rev. D **54**, 1291 (1996) [arXiv:astro-ph/9602031]

[30] M. Christensson, M. Hindmarsh and A. Brandenburg, "Inverse cascade in decaying 3D magnetohydrodynamic turbulence," Phys. Rev. E **64**, 056405 (2001) [arXiv:astro-ph/0011321].

[31] M. Christensson, M. Hindmarsh and A. Brandenburg, "Scaling laws in decaying helical 3D magnetohydrodynamic turbulence," Astron. Nachr. **326**, 393 (2005) [arXiv:astro-ph/0209119].

[32] D. T. Son, "Magnetohydrodynamics of the early universe and the evolution of primordial magnetic fields," Phys. Rev. D **59**, 063008 (1999) [arXiv:hep-ph/9803412]

[33] R. Banerjee and K. Jedamzik, "Are Cluster Magnetic Fields Primordial ?," Phys. Rev. Lett. **91** (2003) 251301; [Erratum-ibid. **93** (2004) 179901] [arXiv:astro-ph/0306211]. R. Banerjee and K. Jedamzik, "The Evolution of Cosmic Magnetic Fields: From the Very Early Universe, to Recombination, to the Present," Phys. Rev. D **70** (2004) 123003; [arXiv:astro-ph/0410032].

[34] T. Vachaspati, "Magnetic fields from cosmological phase transitions," Phys. Lett. B **265**, 258 (1991)

[35] T. Vachaspati, "Electroweak strings, sphalerons and magnetic fields," arXiv:hep-ph/9405286.

[36] T. Vachaspati, "Estimate of the primordial magnetic field helicity," Phys. Rev. Lett. **87**, 251302 (2001) [arXiv:astro-ph/0101261].

[37] T. W. B. Kibble and A. Vilenkin, Phys. Rev. D **52**, 679 (1995).

[38] J. M. Cornwall, "Speculations on primordial magnetic helicity," Phys. Rev. D **56**, 6146 (1997) [arXiv:hep-th/9704022].

[39] E. J. Copeland and P. M. Saffin, "Bubble collisions in Abelian gauge theories and the geodesic rule," Phys. Rev. D **54**, 6088 (1996) [arXiv:hep-ph/9604231].

[40] E. J. Copeland, P. M. Saffin and O. Tornkvist, "Phase equilibration and magnetic field generation in U(1) bubble collisions," Phys. Rev. D **61**, 105005 (2000) [arXiv:hep-ph/9907437].

[41] D. Grasso and A. Riotto, "On the nature of the magnetic fields generated during the electroweak phase transition," Phys. Lett. B **418**, 258 (1998) [arXiv:hep-ph/9707265].

[42] M. Joyce and M. E. Shaposhnikov, "Primordial magnetic fields, right electrons, and the Abelian anomaly," Phys. Rev. Lett. **79**, 1193 (1997) [arXiv:astro-ph/9703005].

[43] M. Giovannini and M. E. Shaposhnikov, "Primordial hypermagnetic fields and triangle anomaly," Phys. Rev. D **57**, 2186 (1998) [arXiv:hep-ph/9710234].

[44] M. S. Turner and L. M. Widrow, "Inflation Produced, Large Scale Magnetic Fields," Phys. Rev. D **37**, 2743 (1988)

[45] B. Ratra, "Cosmological 'seed' magnetic field from inflation," Astrophys. J. **391** (1992) L1

[46] W. D. Garretson, G. B. Field and S. M. Carroll, "Primordial magnetic fields from pseudoGoldstone bosons," Phys. Rev. D **46** (1992) 5346 [arXiv:hep-ph/9209238].

[47] A. Dolgov, "Breaking Of Conformal Invariance And Electromagnetic Field Generation In The Universe," Phys. Rev. D **48** (1993) 2499 [arXiv:hep-ph/9301280].

[48] F. D. Mazzitelli and F. M. Spedalieri, "Scalar electrodynamics and primordial magnetic fields," Phys. Rev. D **52** (1995) 6694 [arXiv:astro-ph/9505140].

[49] M. Novello, L. A. R. Oliveira and J. M. Salim, "Direct Electrogravitational Couplings And The Behavior Of Primordial Large Scale Magnetic Fields," Class. Quant. Grav. **13** (1996) 1089

[50] E. A. Calzetta, A. Kandus and F. D. Mazzitelli, "Primordial magnetic fields induced by cosmological particle creation," Phys. Rev. D **57** (1998) 7139 [arXiv:astro-ph/9707220].

[51] O. Bertolami and D. F. Mota, "Primordial magnetic fields via spontaneous breaking of Lorentz invariance," Phys. Lett. B **455** (1999) 96 [arXiv:gr-qc/9811087].

[52] M. Giovannini and M. E. Shaposhnikov, "Primordial magnetic fields from inflation?," Phys. Rev. D **62**, 103512 (2000) [arXiv:hep-ph/0004269].

[53] M. Giovannini, "Magnetogenesis and the dynamics of internal dimensions," Phys. Rev. D **62**, 123505 (2000) [arXiv:hep-ph/0007163].

[54] A. C. Davis et al., "Primordial spectrum of gauge fields from inflation," Phys. Lett. B **501** (2001) 165 [arXiv:astro-ph/0007214]; K. Dimopoulos et al., "Natural magnetogenesis from inflation," Phys. Rev. D **65** (2002) 063505 [arXiv:astro-ph/0108093].

[55] T. Prokopec and E. Puchwein, "Photon mass generation during inflation: de Sitter invariant case," JCAP **0404** (2004) 007 [arXiv:astro-ph/0312274]; "Nearly minimal magnetogenesis," Phys. Rev. D **70** (2004) 043004 [arXiv:astro-ph/0403335].

[56] K. Enqvist, A. Jokinen and A. Mazumdar, "Seed perturbations for primordial magnetic fields from MSSM flat directions," JCAP **0411** (2004) 001 [arXiv:hep-ph/0404269].

[57] M. R. Garousi, M. Sami and S. Tsujikawa, "Generation of electromagnetic fields in string cosmology with a massive scalar field on the anti D-brane," Phys. Lett. B **606** (2005) 1 [arXiv:hep-th/0405012].

[58] A. Ashoorioon and R. B. Mann, "Generation of cosmological seed magnetic fields from inflation with cutoff," Phys. Rev. D **71** (2005) 103509 [arXiv:gr-qc/0410053].

[59] J. E. Madriz Aguilar and M. Bellini, "Stochastic gravitoelectromagnetic inflation," Phys. Lett. B **642** (2006) 302 [arXiv:gr-qc/0605043].

[60] L. Campanelli et al., "Inflation-Produced Magnetic Fields in Nonlinear Electrodynamics," Phys. Rev. D **77** (2008) 043001 [arXiv:0710.2993 [astro-ph]]; L. Campanelli, "Helical Magnetic Fields from Inflation," arXiv:0805.0575 [astro-ph].

[61] K. Ichiki, K. Takahashi, H. Ohno, H. Hanayama and N. Sugiyama, "Cosmological Magnetic Field: a fossil of density perturbations in the early universe," Science **311**, 827 (2006) [arXiv:astro-ph/0603631]

[62] K. Takahashi, K. Ichiki, H. Ohno and H. Hanayama, "Magnetic field generation from cosmological perturbations," Phys. Rev. Lett. **95**, 121301 (2005) [arXiv:astro-ph/0502283]

[63] R. Durrer "Is the mystery of cosmic magnetic fields solved?" Science **311**, 787 (2006)

[64] E. A. Calzetta and A. Kandus, "Self consistent estimates of magnetic fields from reheating," Phys. Rev. D **65**, 063004 (2002) [arXiv:astro-ph/0110341]

[65] D. Boyanovsky, M. Simionato and H. J. de Vega, "Magnetic field generation from non-equilibrium phase transitions," Phys. Rev. D **67** (2003) 023502 [arXiv:hep-ph/0208272].

[66] D. Boyanovsky, H. J. de Vega and M. Simionato, "Large scale magnetogenesis from a non-equilibrium phase transition in the radiation dominated era," Phys. Rev. D **67** (2003) 123505 [arXiv:hep-ph/0211022].

[67] D. Boyanovsky and H. J. de Vega, "Primordial magnetic fields from out of equilibrium cosmological phase transitions," AIP Conf. Proc. **784**, 434 (2005) [arXiv:astro-ph/0502212].

[68] D. H. Lyth and E. D. Stewart, "Cosmology With A Tev Mass GUT Higgs," Phys. Rev. Lett. **75** (1995) 201 [arXiv:hep-ph/9502417]; "Thermal Inflation And The Moduli Problem," Phys. Rev. D **53** (1996) 1784 [arXiv:hep-ph/9510204].

[69] R. Easther, J. T. Giblin, E. A. Lim, W. I. Park and E. D. Stewart, "Thermal Inflation and the Gravitational Wave Background," arXiv:0801.4197 [astro-ph].

[70] J. Garcia-Bellido, D. Y. Grigoriev, A. Kusenko and M. E. Shaposhnikov, "Non-equilibrium electroweak baryogenesis from preheating after inflation," Phys. Rev. D **60**, 123504 (1999) [arXiv:hep-ph/9902449]; L. M. Krauss and M. Trodden, "Baryogenesis below the electroweak scale," Phys. Rev. Lett. **83**, 1502 (1999) [arXiv:hep-ph/9902420]; J. Garcia-Bellido and D. Y. Grigoriev, "Inflaton-induced sphaleron transitions," JHEP **0001**, 017 (2000) [arXiv:hep-ph/9912515].

[71] G. N. Felder, J. Garcia-Bellido, P. B. Greene, L. Kofman, A. D. Linde and I. Tkachev, "Dynamics of symmetry breaking and tachyonic preheating," Phys. Rev.

Lett. **87**, 011601 (2001) [arXiv:hep-ph/0012142]; G. N. Felder, L. Kofman and A. D. Linde, "Tachyonic instability and dynamics of spontaneous symmetry breaking," Phys. Rev. D **64**, 123517 (2001) [arXiv:hep-th/0106179].

[72] J. M. Cornwall, D. Grigoriev and A. Kusenko, "Resonant amplification of electroweak baryogenesis at preheating," Phys. Rev. D **64** (2001) 123518 [arXiv:hep-ph/0106127]; J. M. Cornwall and A. Kusenko, "Baryon number non-conservation and phase transitions at preheating," Phys. Rev. D **61** (2000) 103510 [arXiv:hep-ph/0001058].

[73] J. Garcia-Bellido, M. Garcia Perez and A. Gonzalez-Arroyo, "Symmetry breaking and false vacuum decay after hybrid inflation," Phys. Rev. D **67**, 103501 (2003) [arXiv:hep-ph/0208228].

[74] J. Garcia-Bellido, M. Garcia-Perez and A. Gonzalez-Arroyo, "Chern-Simons production during preheating in hybrid inflation models," Phys. Rev. D **69**, 023504 (2004) [arXiv:hep-ph/0304285].

[75] J.Smit, A.Tranberg, *JHEP* **12** (2002) 020; *JHEP* **0311** (2003) 016; *JHEP* **0608** (2006) 012; J. I. Skullerud, J. Smit and A. Tranberg, *JHEP* **0308** (2003) 045; M. van der Meulen, D. Sexty, J. Smit and A. Tranberg, *JHEP* **0602** (2006) 029; A. Tranberg, J. Smit and M. Hindmarsh, *JHEP* **0701** (2007) 034.

[76] J. Smit, *Simulations in Early-Universe Theory*, in proceedings of *Lattice 2005 conference*, PoS(LAT2005) 022, and references therein.

[77] J. Garcia-Bellido and D. G. Figueroa, "A stochastic background of gravitational waves from hybrid preheating," Phys. Rev. Lett. **98** (2007) 061302 [arXiv:astro-ph/0701014]; J. Garcia-Bellido, D. G. Figueroa and A. Sastre, "A Gravitational Wave Background from Reheating after Hybrid Inflation," Phys. Rev. D **77** (2008) 043517 [arXiv:0707.0839 hep-ph].

[78] A. Diaz-Gil, J. Garcia-Bellido, M. Garcia Perez and A. Gonzalez-Arroyo, "Magnetic field production during preheating at the electroweak scale," arXiv:0712.4263 [hep-ph], accepted in Phys. Rev. Lett. (2008).

[79] A. Díaz-Gil, J. García-Bellido, M. García Pérez, A. González-Arroyo, in proceedings of *Lattice 2005 conference*, PoS(LAT2005) 242; ibid in proceedings of *Lattice 2007 conference*, PoS(LAT2007) 052.

[80] Particle Data Group, "Review of particle physics," J. Phys. G **33**, 1 (2006), `http://pdg.lbl.gov/`

[81] J. Garcia-Bellido and A. D. Linde, "Preheating in hybrid inflation," Phys. Rev. D **57**, 6075 (1998) [arXiv:hep-ph/9711360].

[82] G. 't Hooft, "Magnetic monopoles in unified gauge theories," Nucl. Phys. B **79** (1974) 276.

[83] C. J. Copi, F. Ferrer, T. Vachaspati and A. Achucarro, "Helical Magnetic Fields from Sphaleron Decay and Baryogenesis," arXiv:0801.3653 [astro-ph].

[84] F. R. Klinkhamer and N. S. Manton, "A Saddle Point Solution In The Weinberg-Salam Theory," Phys. Rev. D **30** (1984) 2212.

[85] R. Micha and I. I. Tkachev, "Relativistic turbulence: A long way from preheating to equilibrium," Phys. Rev. Lett. **90** (2003) 121301 [arXiv:hep-ph/0210202]; "Turbulent thermalization," Phys. Rev. D **70** (2004) 043538 [arXiv:hep-ph/0403101].

[86] J. M. Bardeen, J. R. Bond, N. Kaiser and A. S. Szalay, "The Statistics Of Peaks Of Gaussian Random Fields," Astrophys. J. **304**, 15 (1986).

[87] J. R. Bond, L. Kofman and D. Pogosian, "How Filaments are Woven into the Cosmic Web," Nature **380** (1996) 603 [arXiv:astro-ph/9512141].

[88] J. R. Bond, L. Kofman, D. Pogosian and J. Wadsley, "Theoretical tools for large scale structure," arXiv:astro-ph/9810093; Proceedings of 14th IAP Meeting on Wide Field Surveys in Cosmology (IAP 98), Paris, France, 26-30 May 1998

[89] D. Pogosian, J. R. Bond, L. Kofman and J. Wadsley, "Cosmic Web: Origin and Observables," arXiv:astro-ph/9810072.